Monthly Notices of the ROYAL ASTRONOMICAL SOCIETY

MNRAS **548,** 1–32 (2026) https://doi.org/10.1093/mnras/stag735
Advance Access publication 2026 April 17

Multidimensional nebular-phase calculations of dynamically driven double-degenerate double-detonation models for Type Ia supernovae

J. M. Pollin [1★] S. A. Sim [1,2,3] L. J. Shingles [1,4] R. Pakmor [5] F. P. Callan [1] C. E. Collins [6] F. K. Röpke,[7,8,9] L. A. Kwok,[10] A. Holas[7] and S. Srivastav[11]

[1]*Astrophysics Research Center, School of Mathematics and Physics, Queen's University Belfast, Belfast BT7 1NN, Northern Ireland, UK*
[2]*Cosmic Dawn Center (DAWN), Denmark*
[3]*Niels Bohr Institute, University of Copenhagen, Jagtvej 155A, DK-2200, Copenhagen N, Denmark*
[4]*GSI Helmholtzzentrum für Schwerionenforschung, Planckstraße 1, D-64291 Darmstadt, Germany*
[5]*Max-Planck-Institut für Astrophysik, Karl-Schwarzschild-Str. 1, D-85748, Garching, Germany*
[6]*School of Physics, Trinity College Dublin, The University of Dublin, Dublin 2, Ireland*
[7]*Heidelberger Institut für Theoretische Studien, Schloss-Wolfsbrunnenweg 35, D-69118 Heidelberg, Germany*
[8]*Zentrum für Astronomie der Universität Heidelberg, Institut für Theoretische Astrophysik, Philosophenweg 12, D-69120 Heidelberg, Germany*
[9]*Zentrum für Astronomie der Universität Heidelberg, Astronomisches Rechen-Institut, Mönchhofstr. 12–14, D-69120 Heidelberg, Germany*
[10]*Center for Interdisciplinary Exploration and Research in Astrophysics (CIERA), 1800 Sherman Ave., Evanston, IL 60201, USA*
[11]*Department of Physics, University of Oxford, Denys Wilkinson Building, Keble Road, Oxford OX1 3RH, UK*

Accepted 2026 April 15. Received 2026 April 12; in original form 2025 July 6

ABSTRACT

The dynamically driven double-degenerate double-detonation model has emerged as a promising progenitor candidate for Type Ia supernovae. In this scenario, the primary white dwarf ignites due to dynamical interaction with a companion white dwarf, which may also undergo a detonation. Consequently, two scenarios exist: one in which the secondary survives and another in which both white dwarfs detonate. In either case, substantial departures from spherical symmetry are imprinted on the ejecta. Here, we compute full non-local thermodynamic equilibrium nebular-phase spectra in 1D and 3D to probe the innermost asymmetries. Our simulations reveal that the multidimensional structures significantly alter the overall ionization balance, width, and velocity of features, especially when the secondary detonates. In this scenario, some element distributions may produce orientation-dependent line profiles that can be centrally peaked from some viewing angles and somewhat flat-topped from others. Comparison to observations reveals that both scenarios produce most observed features from the optical to mid-infrared. However, the current model realizations do not consistently reproduce all line shapes or relative strengths, and yield prominent optical Ar III emission which is inconsistent with the data. When the secondary detonates, including 3D effects improves the average agreement with observations, however when compared to observations, particularly weak optical Co III emission and the presence of optical O I and near-infrared S I challenge its viability for normal Type Ia supernovae. Thus, overall, our comparisons with normal Type Ia's tentatively favour detonation of only the primary white dwarf but we stress that more model realizations and mid-infrared observations are needed.

Key words: radiative transfer – methods: numerical – binaries: general – white dwarfs – transients: supernovae.

1 INTRODUCTION

There is general agreement that Type Ia supernovae (SNe Ia) originate from the explosion of a carbon–oxygen (CO) white dwarf (WD; F. Hoyle & W. A. Fowler 1960) in a close binary with a companion. It is still unclear if a WD near the Chandrasekhar mass ($M_{\rm Ch}$) or a sub-Chandrasekhar mass (sub-$M_{\rm Ch}$) progenitor should be favoured for the majority of SNe Ia (see e.g. Z.-W. Liu, F. K. Röpke & Z. Han 2023; A. J. Ruiter & I. R. Seitenzahl 2025, for a review). Additionally, the nature of the WD's companion – whether it is a non-degenerate companion in the single-degenerate scenario (J. Whelan & J. Iben 1973) or another WD in the double-degenerate scenario (J. Iben & A. V. Tutukov 1984) – has remained an open question. There is, however, a growing body of evidence favouring the double-degenerate scenario. The scenario naturally explains several key characteristics: the absence of hydrogen (D. C. Leonard 2007) and the minimal contribution of He in the observed spectra (J.-A. Jiang et al. 2017; U. M. Noebauer et al. 2017; K. De et al. 2019) is easily explained, the rates of the systems are consistent with observed SNe Ia rates

★ E-mail: jpollin02@qub.ac.uk

(A. J. Ruiter, K. Belczynski & C. Fryer 2009), and they can account for the delay-time distribution of SNe Ia (D. Maoz, F. Mannucci & T. D. Brandt 2012).

Investigations of sub-$M_{\rm Ch}$CO WD detonations have demonstrated reasonable agreement with observations of SNe Ia (S. A. Sim et al. 2010; S. Blondin et al. 2017; K. J. Shen et al. 2018a, 2021). These models have reproduced several key observational features, such as the width–luminosity relation (M. M. Phillips 1993). However, the unknown nature of the companion introduces a significant amount of uncertainty regarding the detonation mechanism. Among the possible mechanisms, the double-detonation scenario has garnered significant interest; a detonation is ignited in the helium surface layer on the WD, which sends shockwaves inward, triggering the detonation of the underlying CO core (K. Nomoto 1980; R. E. Taam 1980; E. Livne 1990; P. Hoeflich & A. Khokhlov 1996; P. Nugent et al. 1997). Moreover, high-resolution observations of a supernova remnant provide strong support for this mechanism (P. Das et al. 2025); however, see N. Soker (2025) for an alternative perspective.

It is particularly noteworthy that modern double-detonation models (L. Bildsten et al. 2007; K. J. Shen & L. Bildsten 2009; M. Fink et al. 2010; M. Kromer et al. 2010; K. J. Shen et al. 2010; A. Polin, P. Nugent & D. Kasen 2019; D. M. Townsley et al. 2019; S. Gronow et al. 2020, 2021; S. J. Boos et al. 2021; K. J. Shen, S. J. Boos & D. M. Townsley 2024) have demonstrated a continued ability to achieve CO detonations with lower mass helium shells compared to those used in earlier models (E. Livne 1990; E. Livne & A. S. Glasner 1990; E. Livne & D. Arnett 1995). The synthetic observables of double-detonation models have also come into better agreement with observations, due to these smaller helium shells, and, as such, the double-detonation mechanism remains a subject of active investigation.

Given the aforementioned motivations for favouring the double-degenerate channel and the success of the double-detonation mechanism, it has been of particular interest to apply the mechanism to a dynamically driven double-degenerate merger scenario. In this scenario, the primary WD undergoes dynamical helium accretion from the secondary WD before the merger. The instabilities in the helium accretion stream result in a thermonuclear runaway in the helium shell, leading to the double-detonation of the primary (J. Guillochon et al. 2010; R. Pakmor et al. 2013, 2022; R. Kashyap et al. 2015; A. Tanikawa, K. Nomoto & N. Nakasato 2018; J. Morán-Fraile et al. 2024). An essential difference between the double-degenerate double-detonation scenario and the classic violent merger scenario (R. Pakmor et al. 2012) or the helium-ignited violent merger model (R. Pakmor et al. 2013; A. Tanikawa et al. 2015) lies in the timing of the detonation. In the violent merger scenario, the secondary is disrupted during the merging of the CO cores. Whereas in the dynamically driven double-degenerate double-detonation (D^6) scenario a detonation occurs at the earliest possible stage of the merger during the phase of rapid accretion of helium-rich material from the outer layer of the secondary before it is disrupted.

There currently exists only a handful of D^6 models. As such, significant uncertainties persist regarding the fate of the secondary WD, which is intact at the time of the primary WD's detonation (A. Tanikawa et al. 2019; R. Pakmor et al. 2022; S. J. Boos, D. M. Townsley & K. J. Shen 2024). There are two key open questions surrounding the system's dynamics: first, the role of the accretion stream and how the helium shell detonation affects the temperature and density of the primary WD; and secondly, the conditions of the secondary WD at the point of shock convergence. Notably, R. Pakmor et al. (2022) performed two 3D hydrodynamic simulations, tracking the initial inspiral, mass transfer, helium shell detonation, and subsequent WD core detonation. In one simulation, only the primary detonates, and the secondary survives. in the other simulation, both the primary and secondary WDs ignite and explode.

It was demonstrated that the two simulations produced remarkably similar spectra (using 1D radiative transfer simulations) in the photospheric phase (R. Pakmor et al. 2022). This overall similarity was confirmed by subsequent 3D simulations for these models (J. M. Pollin et al. 2024), and is supported by the 2D models of S. J. Boos et al. (2024). In the 3D calculation, the primary difference between the two models was more considerable variation with viewing angle of the synthetic observables, such as luminosity, spectral features, and colour evolution when the secondary WD detonated. Similar to idealized double-detonation model calculations (C. E. Collins et al. 2022; A. Holas et al. 2025), it was found that although the spread in these observables is significant compared to observational data, it remains insufficient to rule out this explosion pathway. Moreover, this spread may be reduced with lower helium shell masses and full non-local thermodynamic equilibrium (NLTE) calculations (C. E. Collins et al. 2025).

A striking consequence of WD merger models where the secondary WD is also disrupted is the formation of an 'inner bubble' structure within the ejecta (see Fig. 1).[1] As this 'inner bubble' and other core asymmetries are located in the innermost ejecta, they significantly influence synthetic observables once the ejecta has expanded sufficiently to allow spectra from the central ejecta to emerge in the nebular phase. Thus, to understand the impact of this inner structure, it is essential to investigate the late phase ($\sim$ 1 yr after the explosion). At this epoch, excitation by both radiative and collisional processes becomes slow, and only the lowest energy states possess significant populations. Hence, forbidden emission, particularly from Fe, Co, and Ni, dominate (J. Spyromilio et al. 1992).

Late-phase observations have revealed that SNe Ia features show some degree of blueshift or redshift from their rest wavelengths (K. Motohara et al. 2006; C. L. Gerardy et al. 2007; K. Maeda et al. 2010; K. Maguire et al. 2018; A. Flörs et al. 2020). It has been suggested that these shifts could be a result of off-centre ignition (K. Maeda et al. 2010). A 3D off-centre detonation will inherently lead to an asymmetric distribution of the ejecta (A. Holas et al. 2025). Moreover, the distribution of ejecta can not only lead to different velocities but also different widths and line profiles of features. For a comprehensive review of the effect of different ejecta configurations on line profiles, see A. Jerkstrand (2017). The optical region is complicated by blending of multiple species, and many ground-based observations are hindered by telluric absorption. However, the launch of the *James Webb Space Telescope* (*JWST*) has provided an unprecedented opportunity to explore the mid-infrared (MIR) region, where features are more isolated. Of particular interest is SN 2021aefx (L. A. Kwok et al. 2023), which was observed at $\sim$270 d post-explosion using the South African Large Telescope (SALT) and, notably, *JWST*. As such, observations of SN 2021aefx at this epoch span from the optical, near-infrared (NIR)

[1] This 'inner bubble' feature is also present in the model by R. Pakmor et al. (2012), suggesting it may be representative of WD mergers more broadly.

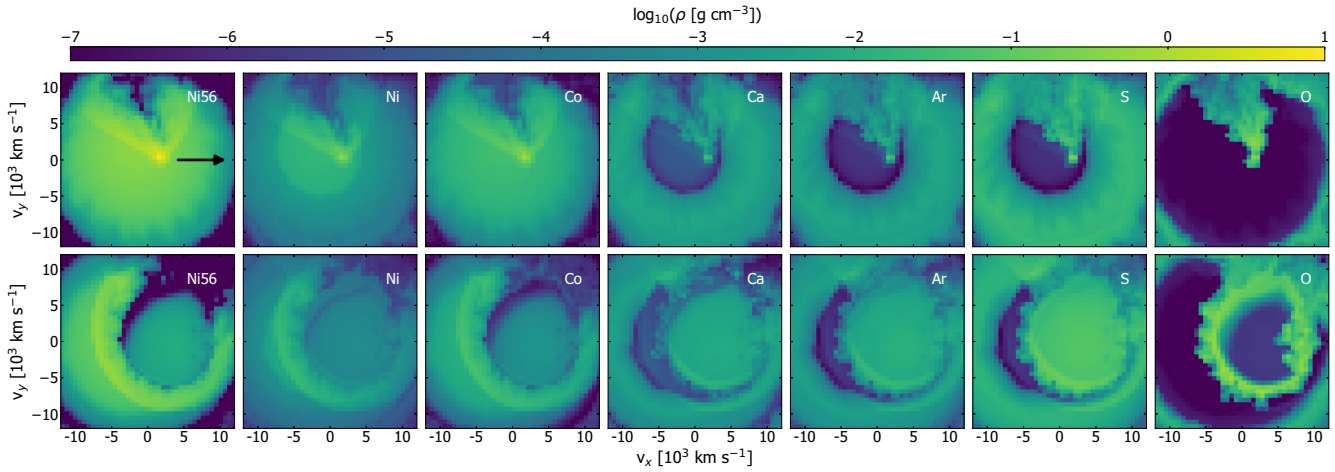

Figure 1. Density of key species in the 3DOneExpl (top) and 3DTwoExpl (bottom) models, in the X–Y plane at $\cos(\theta) = 0$ where the arrow in the top-left panel indicate the direction of $\phi = 0°$. The scale indicates the logarithmic density of each species. Note this snapshot is at 270 d after explosion, apart from ^{56}Ni, which is shown at 0.002 d.

and MIR (0.35–14 μ m) This ample wavelength coverage enables a more reliable investigation of ejecta stratification, which can be used to assess different progenitor scenarios and explosion mechanisms.

Since the one-zone models of T. S. Axelrod (1980), there have been many theoretical studies exploring multizone models of nebular SNe Ia (e.g. P. Ruiz-Lapuente & L. B. Lucy 1992; W. Liu, D. J. Jeffery & D. R. Schultz 1997; P. A. Mazzali et al. 2001, 2020; P. Höflich et al. 2004; C. Kozma et al. 2005; I. Maurer et al. 2011; C. Li, D. J. Hillier & L. Dessart 2012; T. R. Diamond, P. Hoeflich & C. L. Gerardy 2015; C. Fransson & A. Jerkstrand 2015; J. Botyánszki & D. Kasen 2017; L. J. Shingles et al. 2020, 2022; A. Polin, P. Nugent & D. Kasen 2021; S. Blondin et al. 2023). These investigations have enhanced our understanding of the geometry and composition of SNe Ia. While many of these have relied on assumptions of spherical symmetry or optically thin emission, which may not fully capture the complexity of the ejecta conditions (e.g the line shifts and morphologies), they have none the less provided valuable insights. Several investigations have strived to overcome these limitations by employing various methods, such as using simplified geometries (e.g. K. Maeda et al. 2010) or superposition of 1D models (e.g. P. A. Mazzali et al. 2018). While these approaches have provided valuable insights, they remain constrained by their simplifications. As noted by R. Pakmor et al. (2024), there is an ever-growing need to perform 3D nebular-phase calculations, since modern explosion models are fundamentally multidimensional. Given the large departures from spherical symmetry in D^6 models developed, nebular-phase spectra are expected to show significant asymmetries. Hence, 3D NLTE nebular calculations are necessary to accurately model this scenario and reconcile synthetic observables with observed properties of SNe Ia.

In this work, we build upon the photospheric-phase calculations of R. Pakmor et al. (2022) and J. M. Pollin et al. (2024), extending our investigation to the deepest regions of the ejecta, hundreds of days after the explosion, in 3D. Section 2 outlines the models and the radiative transfer configuration. Section 3.1 presents the angle-averaged spectra and compares them with the corresponding spherically averaged spectra. Sections 3.2 and 3.3 explore the orientation effects for each explosion model. Throughout this work, we compare the D^6 models across the optical, NIR and MIR to the spectroscopically normal SN 2021aefx (L. A. Kwok et al. 2023). Finally, we discuss our findings and present conclusions in Section 4.

2 METHODS

2.1 Hydrodynamical ejecta models

The two hydrodynamical explosion models investigated in this work are the 3D models from R. Pakmor et al. (2022). The first is where only the primary WD explodes and the secondary survives (3DOneExpl) and the second is where both WDs explode (3DTwoExpl). These models originate from a binary system consisting of a primary CO WD with a mass of 1.05 $M_\odot$ and a secondary CO WD with a mass of 0.7 $M_\odot$. In both scenarios, the WDs have a thin helium shell of 0.03 $M_\odot$, which is dynamically transferred from the secondary WD to the primary WD (for detailed nucleosynthesis, see R. Pakmor et al. 2022). The abundance structures of key species relevant to the nebular-phase for both models are presented in Fig. 1. To highlight the importance of multidimensional radiative transfer effects in the nebular phase, we also performed corresponding 1D calculations of both scenarios. To impose spherical symmetry, these 1D models were constructed by averaging the 3D hydrodynamical simulations across 100 spherical shells. The resulting 1D explosion models are referred to as the 1DOneExpl and 1DTwoExpl models. For clarity, when referring to the 3DOneExpl and 1DOneExpl models or the 3DTwoExpl and 1DTwoExpl models collectively, we describe them as the OneExpl scenario and TwoExpl scenario, respectively.

2.2 Radiative transfer

We perform our radiative transfer calculations using the 3D Monte Carlo radiative transfer code ARTIS (S. A. Sim 2007; M. Kromer & S. A. Sim 2009). The methods used by ARTIS are based on L. B. Lucy (2002, 2003, 2005), which divides the radiation field into indivisible Monte Carlo packet quanta. This work utilizes the full NLTE approach developed by L. J. Shingles et al. (2020), which includes an NLTE population and ionization solver and

treatment of non-thermal leptons. To follow the population of leptons with non-thermally distributed energies, ARTIS solves the Spencer–Fano equation (as formulated by C. Kozma & C. Fransson 1992). Treatment of all levels in NLTE for every ion has a significant memory and computational cost. As such, we restrict the number of NLTE levels. For most ions, we treat the first 80 levels in NLTE but increase this to 197 NLTE levels for Fe II to ensure all metastable levels are treated in NLTE. We place other levels into an additional NLTE level that can vary in population, known as a 'superlevel' (L. S. Anderson 1989); the absolute population of the superlevel is determined by the NLTE solver, while the relative populations of the stages within the superlevel are set by a Boltzmann distribution at the electron temperature.[2] We also include the heating, ionization, and excitation due to Auger electrons from ionizations of inner shells.

The atomic data used in our calculations are based on the compilation of CMFGEN (D. J. Hillier 1990; D. J. Hillier & D. L. Miller 1998) and is the same as that used by L. J. Shingles et al. (2022). Employing a detailed treatment (L. B. Lucy 2003) for all photoionization processes is memory-intensive in 3D. As such, in this work we adopt a new hybrid scheme for calculating photoionization rate estimators, where the detailed treatment is used for bound–free transitions whose lower levels are included in the NLTE solution and the integral over the binned radiation-field model (L. J. Shingles et al. 2020) for all others.[3]

We employ the ejecta profiles once homologous expansion has been established, which typically occurs ∼100 s after the explosion. In R. Pakmor et al. (2022), the simulations were evolved for more than 100 s past ignition to ensure that this condition is satisfied. We then map this homologously expanding ejecta to 230 d past explosion. Our simulation utilizes 60 logarithmically spaced time-steps from 230 to 305 d post-explosion. We simulate photons produced within the ejecta during this epoch. Given the ∼25-d light-crossing time for the line-forming region of the ejecta, our calculations accurately represent the observable emission between 250 and 279 d. The simulations are initialized in LTE for the first 8 time-steps, after which the full NLTE treatment is activated. We find that the plasma state converges rapidly once the calculation departs from LTE, with convergence achieved by time-step 12. After time-step 12, the plasma properties evolve only gradually between successive steps. These calculations use 3.07×10^{10} Monte Carlo packets, and transport is performed on a 3D Cartesian grid that co-expands with the ejecta. The calculations carried out here maintain the same grid resolution as those by J. M. Pollin et al. (2024), but we exclude cells with absolute Cartesian velocities which exceed 12 000 km s^{-1}. This adjustment preserves the inner ejecta while removing the outermost cells, which have minimal impact on the nebular spectra because the fast, diffuse outer ejecta have low densities and receive little to no energy deposition at these epochs.[4]

To investigate angle-averaged synthetic observables we use all emergent packets to make the angle-averaged spectra (see Section 3.1). To examine specific lines of sight (see Sections 3.2 and 3.3), we use the virtual packet scheme developed by M. Bulla, S. A. Sim & M. Kromer (2015). This enhances signal-to-noise ratio for selected viewing angles. We stress that the computational overhead for the virtual packets in the nebular phase is negligible compared to the NLTE solver cost. The virtual packets are enabled for the entire calculation and are active between 0.35–30 μ m. We have enabled virtual packets for 30 orientations, corresponding to $\cos\theta = 0.0, 0.4, 0.8$, with 10 equally spaced ϕ angles ranging from 0–360°, where θ is the angle from the positive z-axis, and ϕ is the degree of rotation of the projection in the xy-plane. Hence, rotation of ϕ occurs anticlockwise from $\phi = 0°$ and is indicated by the directional arrow in Fig. 1. In this work, we focus on the merger plane ($\cos\theta = 0.0$), where both the 3DOneExpl and 3DTwoExpl models exhibit the most significant variations in density and temperature. These differences lead to the most significant variations in synthetic observables; consequently, we exclude the $\cos\theta = 0.4$ and 0.8 angles from our detailed analysis.[5]

3 RESULTS

In Section 3.1, we examine the spherically averaged and angle-averaged spectra and in Sections 3.2 and 3.3, we explore the orientation effects for the 3DOneExpl and 3DTwoExpl models, respectively. To facilitate detailed comparisons, we have divided the spectra into three key wavelength regions, following the same terminology of S. Blondin et al. (2023): the optical (0.35–1 μ m), the NIR (1–5 μ m), and the MIR (5–30 μ m).

3.1 Angle-averaged spectra

We begin our analysis of the D^6 scenario by examining the signatures from the 1D models and the angle-averaged signatures from 3D models, as shown in Fig. 2. Following the approach of L. A. Kwok et al. (2023) and S. Blondin et al. (2023), we present the spectra in flux per unit frequency rather than per unit wavelength. This improves visual clarity and facilitates more direct comparisons between models and observations across the entire wavelength range (see Table 1 for a detailed breakdown of the flux distribution across different regions). We also summarize some of the prominent spectral lines observed in SNe Ia in Table 2.[6]

To enable a quantitative comparison between the models, we use the Monte Carlo packet data to identify the emitting regions associated with the transitions listed in Table 2. For each transition, we determine the full width at zero intensity, defining the wavelength interval over which the feature merges into the background, and integrate both the transition-specific flux and the total flux within this interval, and compute the contribution of the transition to the overall emission in that wavelength range. This provides a direct measure of the degree to which features are blended. We emphasize that this metric is not normalized to SN 2021aefx, as a normalization would not provide

[2]For the calculations presented in Section 3, we find that the superlevel populations are typically many orders of magnitude lower than the corresponding ground-state populations, for both IGE and IME. We therefore reaffirm that the superlevel approximation remains a valid and appropriate approach.
[3]See Appendix A for an overview of this hybrid scheme for calculating photoionization rate estimators.
[4]See Appendix B for a discussion on the effects of removing the outer cells in a 25^3 model.
[5]See Appendix C for representative cases for a selected ϕ at $\cos\theta = 0, 0.4$, and 0.8
[6]In this work, we refer to nebular features using the gf-weighted mean wavelength, while for plotting purposes we mark the strongest transition.

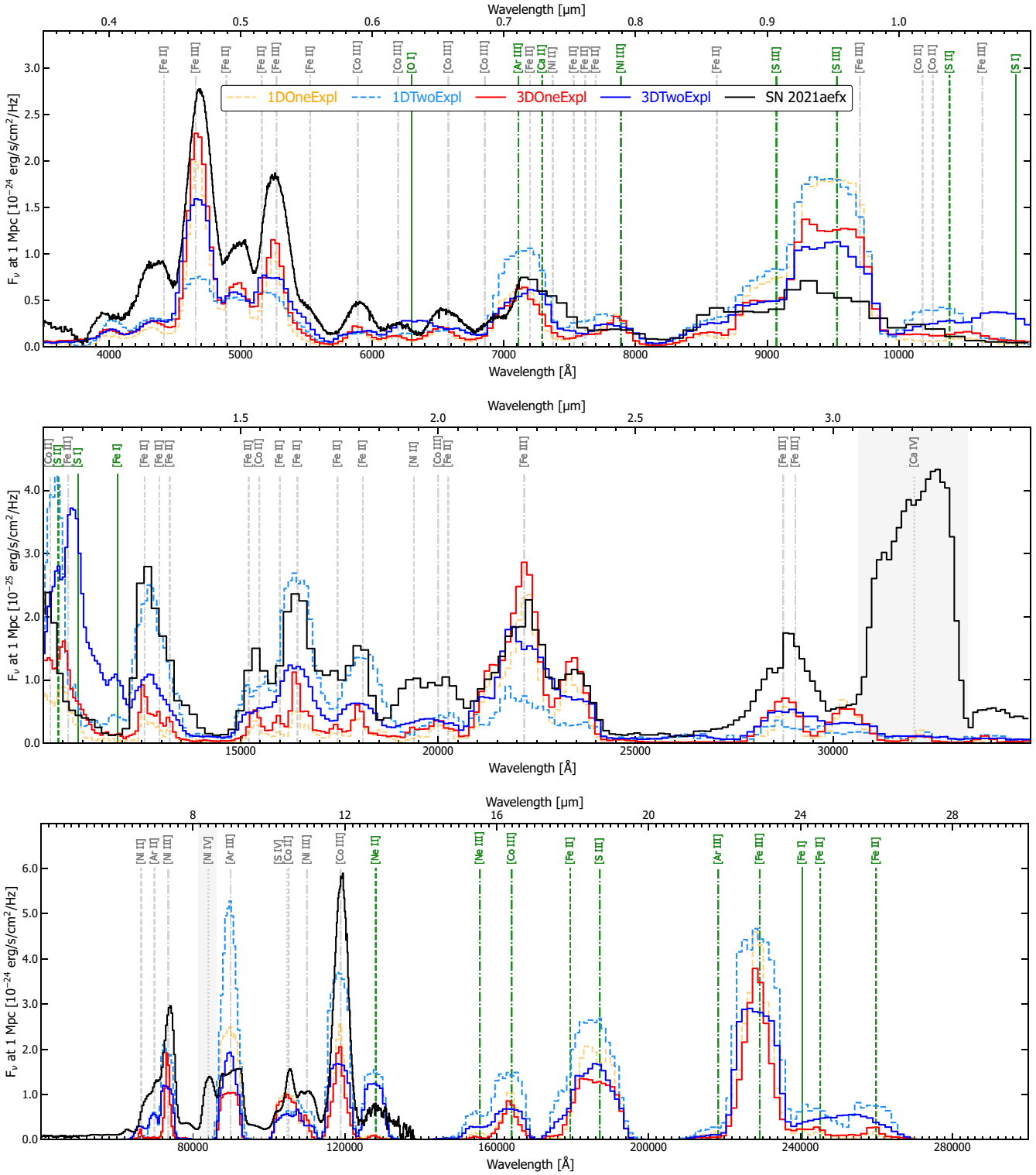

Figure 2. 1D and angle-averaged 3D optical (top; ∼0.35–1 μm), NIR (middle; ∼1–4 μm), and MIR (bottom; ∼4–30 μm) spectra for the 1DOneExpl, 1DTwoExpl, 3DOneExpl, and 3DTwoExpl models at 270 d post-explosion, compared to SN 2021aefx. Observed spectra are corrected for redshift and extinction (G. Hosseinzadeh et al. 2022), and all spectra are scaled to a distance of 1 Mpc. Vertical grey lines indicate the rest wavelengths of prominent features identified by A. Flörs et al. (2020) and L. A. Kwok et al. (2023). In contrast, green lines highlight significant model features that diverge from observations and lie outside the spectral range of SN 2021aefx. The line styles of the vertical lines indicate ionization stages: solid for neutral species, dashed for singly ionized, dash–dotted for doubly ionized, and dotted for triply ionized species. Rest wavelengths identified for SN 2021aefx by L. A. Kwok et al. (2023) are listed in Table 2, where we assess the presence (or absence) of species and the degree to which they are blended. Note that the shaded grey regions highlight prominent features that we do not reproduce due to their absence in our atomic data.

Table 1. Flux distribution ratios across the optical, NIR, and lower MIR bands for each model and SN 2021aefx (L. A. Kwok et al. 2023). The ratios are calculated by integrating $F_\lambda \mathrm{d}\lambda$ over the full observed spectrum and then normalising to the total contribution from all bands.

Range	1DOneExpl	3DOneExpl	1DTwoExpl	3DTwoExpl	SN 2021aefx
Optical (0–1 μm)	0.90	0.91	0.80	0.84	0.86
NIR (1–5 μm)	0.03	0.04	0.07	0.07	0.06
Lower MIR (>5–14 μm)	0.07	0.05	0.13	0.09	0.08

Table 2. Prominent emission lines of SN 2021aefx across the optical, NIR, and MIR wavelength ranges (see L. A. Kwok et al. 2023). Following the notation of L. A. Kwok et al. (2023), a '?' denotes tentatively identified transitions in the observations. To evaluate the synthetic spectra for the 1DOneExpl, 3DOneExpl, 1DTwoExpl, and 3DTwoExpl models, we use Monte Carlo packet information to determine whether a given transition is present. For each line, we identify the observer-frame wavelength interval over which packets are tagged as having their last interaction with that transition. This interval defines the full width at zero intensity, representing the wavelength range where the feature merges into the background and provides a measure of overall blending. We then compute the total transition specific integrated flux across this wavelength interval and report it at a distance of 1 Mpc. To assess the relative strength of the feature, we then express the contribution of the transition specific integrated flux as a percentage of the total integrated flux within the same interval at the same distance, in order to examine a feature's overall purity. A × denotes the absence of the species in the synthetic spectra, while a ○ indicates that the feature is missing owing to its absence from our atomic data set; in such cases, no conclusion regarding its physical presence or absence should be drawn.

		1DOneExpl		3DOneExpl		1DTwoExpl		3DTwoExpl	
λ_{rest}	Species	Flux (erg s^{-1} cm^{-2})	Per cent	Flux (erg s^{-1} cm^{-2})	Per cent	Flux (erg s^{-1} cm^{-2})	Per cent	Flux (erg s^{-1} cm^{-2})	Per cent
				Optical + NIR					
0.589	[Co III]	2.4×10^{-23}	48.7	2.3×10^{-23}	29.4	2.7×10^{-23}	33.9	2.4×10^{-23}	31.2
0.716	[Fe II]	0.9×10^{-23}	3.6	1.6×10^{-23}	6.9	4.5×10^{-23}	9.0	2.1×10^{-23}	6.4
0.738	[Ni II]	0.4×10^{-24}	0.4	4.0×10^{-24}	2.8	1.6×10^{-24}	0.9	9.7×10^{-24}	4.4
1.257	[Fe II]	1.0×10^{-23}	57.2	1.9×10^{-23}	46.2	9.6×10^{-23}	43.0	3.8×10^{-23}	48.1
1.547	[Co II]	0.9×10^{-24}	11.0	2.9×10^{-24}	10.3	5.7×10^{-24}	6.6	4.2×10^{-24}	6.7
1.644	[Fe II]	1.7×10^{-23}	56.9	3.1×10^{-23}	49.4	1.5×10^{-22}	57.3	6.1×10^{-23}	50.7
1.939	[Ni II]	0.5×10^{-24}	27.6	5.5×10^{-24}	21.9	0.2×10^{-24}	17.1	1.0×10^{-23}	15.7
2.219	[Fe III]	9.3×10^{-23}	56.1	1.3×10^{-22}	52.9	4.8×10^{-23}	41.6	1.0×10^{-22}	39.9
2.874	[Fe III]	3.3×10^{-24}	31.7	6.2×10^{-24}	18.6	1.1×10^{-24}	14.3	7.5×10^{-24}	13.4
2.905	[Fe III]	2.0×10^{-23}	20.3	1.8×10^{-23}	26.2	2.1×10^{-23}	72.7	3.0×10^{-23}	42.1
				MIR					
6.636	[Ni II]	0.6×10^{-23}	100	3.1×10^{-22}	87.5	1.7×10^{-22}	57.8	8.6×10^{-22}	60.7
6.985	[Ar II]	1.1×10^{-22}	45.5	1.3×10^{-22}	32.8	1.5×10^{-21}	40.8	1.5×10^{-21}	32.7
7.349	[Ni III]	3.1×10^{-21}	99.0	3.0×10^{-21}	96.7	6.0×10^{-21}	92.8	4.0×10^{-21}	89.3
8.405	[Ni IV]	○	○	○	○	○	○	○	○
8.991	[Ar III]	1.3×10^{-20}	100	0.6×10^{-20}	99.8	2.3×10^{-20}	99.9	0.9×10^{-20}	99.7
10.510	[S IV]	5.6×10^{-21}	85.4	5.2×10^{-21}	69.1	3.1×10^{-21}	57.6	2.9×10^{-21}	57.8
10.521	[Co II]	0.3×10^{-22}	7.9	2.6×10^{-22}	5.0	6.1×10^{-22}	15.3	4.8×10^{-22}	12.9
11.002	[Ni III]	0.8×10^{-21}	45.7	1.1×10^{-21}	68.6	2.6×10^{-21}	17.9	1.5×10^{-21}	20.7
11.888	[Co III]	0.8×10^{-20}	97.1	0.7×10^{-20}	96.4	2.0×10^{-20}	79.0	1.0×10^{-20}	89.5
				Tentative					
2.911	[Ni II]?	1.1×10^{-24}	10.1	0.9×10^{-24}	1.5	×	×	0.8×10^{-24}	1.7
3.044	[Fe III]?	5.4×10^{-23}	94.6	5.4×10^{-23}	70.3	1.4×10^{-23}	60.5	3.5×10^{-23}	51.7
6.214	[Co II]?	○	○	○	○	○	○	○	○
6.920	[Ni II]?	×	×	×	×	×	×	7.7×10^{-24}	0.7
7.791	[Fe III]?	5.6×10^{-23}	87.3	6.5×10^{-23}	81.4	3.7×10^{-23}	76.2	6.9×10^{-23}	59.9
10.682	[Ni II]?	×	×	4.8×10^{-23}	1.0	3.0×10^{-23}	1.0	8.9×10^{-23}	2.5
11.167	[Co II]?	1.6×10^{-23}	49.0	0.4×10^{-23}	1.5	1.7×10^{-23}	3.6	1.5×10^{-23}	1.1
12.729	[Ni II]?	×	×	3.7×10^{-23}	14.2	2.3×10^{-23}	2.7	8.3×10^{-23}	1.5

a consistent basis for comparison across different SNe Ia. Consequently, while this approach quantifies the relative contribution of a transition within a given wavelength range, it does not by itself determine whether a feature would be detectable in a particular observed spectrum. We therefore also report the total integrated flux of the specific transition under consideration in order to aid assessment of whether the transition would be detectable in an observed spectrum. Note that the synthetic spectrum should also be considered when assessing the detectability of a particular feature and the possible contribution of other

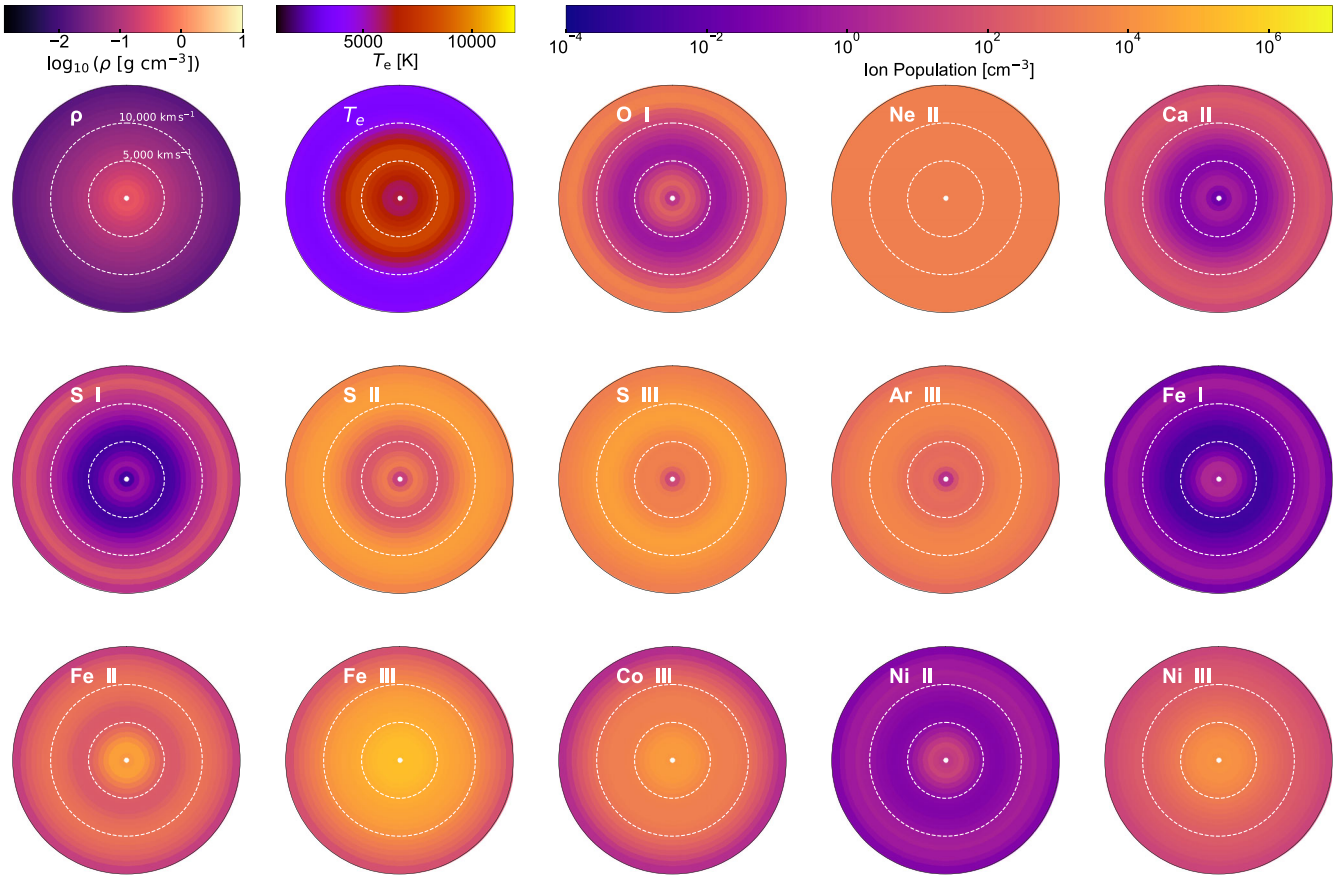

Figure 3. Ejecta properties for the 1DOneExpl model at 270 d. Each panel shows the 2D projection of the 1D property as a function of radial velocity: mass density (ρ), electron temperature (T_e), and ion populations of key species (O I, Ne II, Ca II, S I–III, Ar III, Fe I–III, and Ni II–III). All panels share a common radial velocity scale, with inner and outer dashed circles marking velocities of 5000 and 10 000 km s^{-1}, respectively. Colour bars are consistent with those in Figs 4–6, enabling direct comparison of ejecta properties between the 1D and 3D models. Note that a small fraction of cells (∼1 per cent) possess populations below 10^{-4} and are clipped to this value to improve the overall clarity and allow for clearer comparisons.

transitions within the same wavelength interval.[7] Overall, the explosion models recover many of the transitions reported by L. A. Kwok et al. (2023); however, substantial blending remains evident across several wavelength intervals, particularly in the optical and NIR, while blending generally decreases towards longer wavelengths.

To better understand the differences between the 1D and 3D models we have extracted key physical properties from the models and radiative transfer calculations in Figs 3–6. These figures display the following physical quantities: density (ρ), the electron temperature (T_e), and ion populations (O I, Ne II, Ca II, S I–III, Ar III, Fe I–III, Co III, and Ni II–III). For the 1D models, which represent spherical symmetry, we project the extracted properties into 2D, for ease of visual comparison. For the 3D calculations, we extract a 2D slice through the merger plane. The multidimensional treatments display significant deviations from spherical symmetry in their respective ion distributions, with the 3DTwoExpl model exhibiting more pronounced asymmetries than the 3DOneExpl model.

[7]Note that the synthetic spectrum may also display emission from the same ionization stage; however, the values presented in Table 2 specifically evaluate the presence of the specified transitions identified by L. A. Kwok et al. (2023).

Despite the secondary WD detonation significantly altering the explosion geometry, both scenarios yield broadly similar angle-averaged synthetic spectra, although neither reproduces all observed features of SN 2021aefx at the correct strengths. The different profiles arise due to different geometries and chemical stratifications. As such, line profiles can appear broad and flat-topped (e.g. the Ar III 8.991 μm feature in the 3DOneExpl model), narrow and centrally peaked (e.g. the Co III 11.888 μm feature in the 3DOneExpl model), or a blend of both (e.g. the Fe III 22.925 μm feature in the 3DTwoExpl model). We emphasize, however, that the angle-averaged spectrum represents a superposition of multiple viewing angles and does not correspond to any one line-of-sight from the 3D calculation. Consequently, the morphology of a feature in the averaged 3D spectrum must be interpreted with caution. For example, a broad or flat-topped profile does not uniquely imply emission from a geometrically thin shell, but may instead arise from intrinsically narrower features whose line centres shift with observer orientation. This effect is particularly important for iron-group elements (IGEs), such as Co III, in the 3DTwoExpl model, where significant velocity offsets between viewing angles can artificially impact the averaged profile but are also important for intermediate-mass elements (IMEs), such as Ar III. For this reason, direct comparisons of line shapes between 1D models and angle-averaged 3D models can be misleading. Instead, the integrated line flux provides a more robust diagnostic,

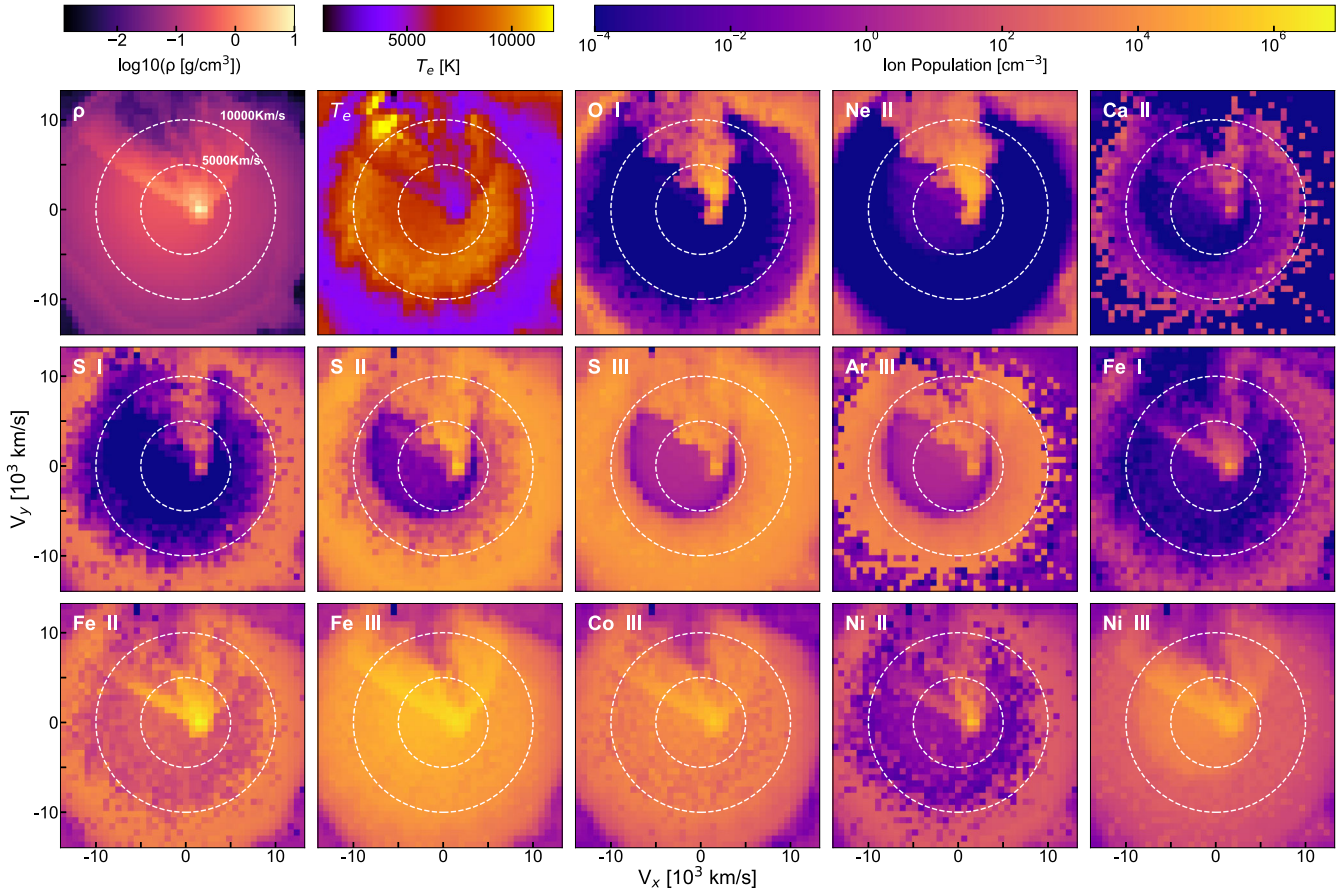

Figure 4. Ejecta properties for a slice ($\cos(\theta) = 0$; i.e. the merger plane) through the 3DOneExpl model at 270 d. Each panel shows a 2D slice of the 3D ejecta mapped into velocity space, displaying: mass density (ρ), electron temperature (T_e), and ion populations of key species (O I, Ne II, Ca II, S I–III, Ar III, Fe I–III, and Ni II–III). Dashed circles mark radial velocities of 5000 and 10 000 km s^{-1}. Colour bars match those in Figs 3, 5, and 6, enabling consistent comparison between 1D and 3D models. We note a small fraction of cells (∼1 per cent) have ion populations below 10^{-4}. These ion populations are clipped at this threshold, as such low populations have a negligible impact on the spectra. Additionally, some (∼0.3 per cent) outer (>10 000 km s^{-1}) cells in low-density regions possess temperatures above 12 000 K. As such, we also clip these cell temperatures to this value to improve the overall clarity and allow for clearer comparisons.

as in optically thin ejecta, it should be independent of viewing angle, except in wavelength regions where residual optical depth effects remain important.

To place our results in context, we compare to the normal SN 2021aefx (L. A. Kwok et al. 2023) at 270 d post-explosion during its nebular phase. The observational data have been corrected for a redshift of $z = 0.005017$ and for reddening due to host galaxy extinction, $E(B-V)_{\rm host} = 0.097$ mag (G. Hosseinzadeh et al. 2022), as well as Milky Way extinction, $E(B-V)_{\rm MW} = 0.008$ mag (E. F. Schlafly & D. P. Finkbeiner 2011). We note that the reported peak B-band magnitude of SN 2021aefx ranges from −19.28 (C. Ashall et al. 2022) to −19.62 (G. Hosseinzadeh et al. 2022). For further details on the data calibration and collection of the nebular spectrum, see L. A. Kwok et al. (2023). As noted by S. Blondin et al. (2023), the distance uncertainty of ∼2 Mpc leads to inferred ^{56}Ni masses ranging from $\lesssim 0.6$ to $> 0.8\,{\rm M}_\odot$. Both explosion scenarios considered here produce nearly identical ^{56}Ni yields, as this is primarily set by the mass of the primary WD. The OneExpl and TwoExpl scenarios possess 0.45 and 0.46 $\rm M_\odot$ of ^{56}Ni, respectively. After removing the line-blanketing effects of the helium shell detonation, the peak B-band magnitudes of the 3DOneExpl and 3DTwoExpl models are −19.04 and −19.26, respectively (J. M. Pollin et al. 2024). However, these correspond to only a few lines of sight; on average, our explosion models are expected to be slightly too faint to match SN 2021aefx. We note that S. Blondin et al. (2023) considered models with ^{56}Ni masses in the range 0.5–0.8 $\rm M_\odot$ as suitable progenitor candidates for SN 2021aefx. Therefore, our models are only marginally fainter than those considered in previous investigations.

3.1.1 *Optical comparison*

The optical spectra of both explosion models are dominated by doubly ionized species, including Fe III, Ar III, S III, Co III, and Ni III, with additional contributions from singly ionized elements such as Fe II and Co II. All models produce distinct features broadly resembling those observed, and in most cases reproduce the relative strengths of the dominant transitions. The spectra of the 3DOneExpl and 1DOneExpl models shown in Fig. 2 are broadly similar, although quantitative differences are evident. For example, the integrated line flux of the Fe III 0.470 μm feature in the 3D calculation is approximately 17 per cent larger than in the corresponding 1D model. Moreover, IME

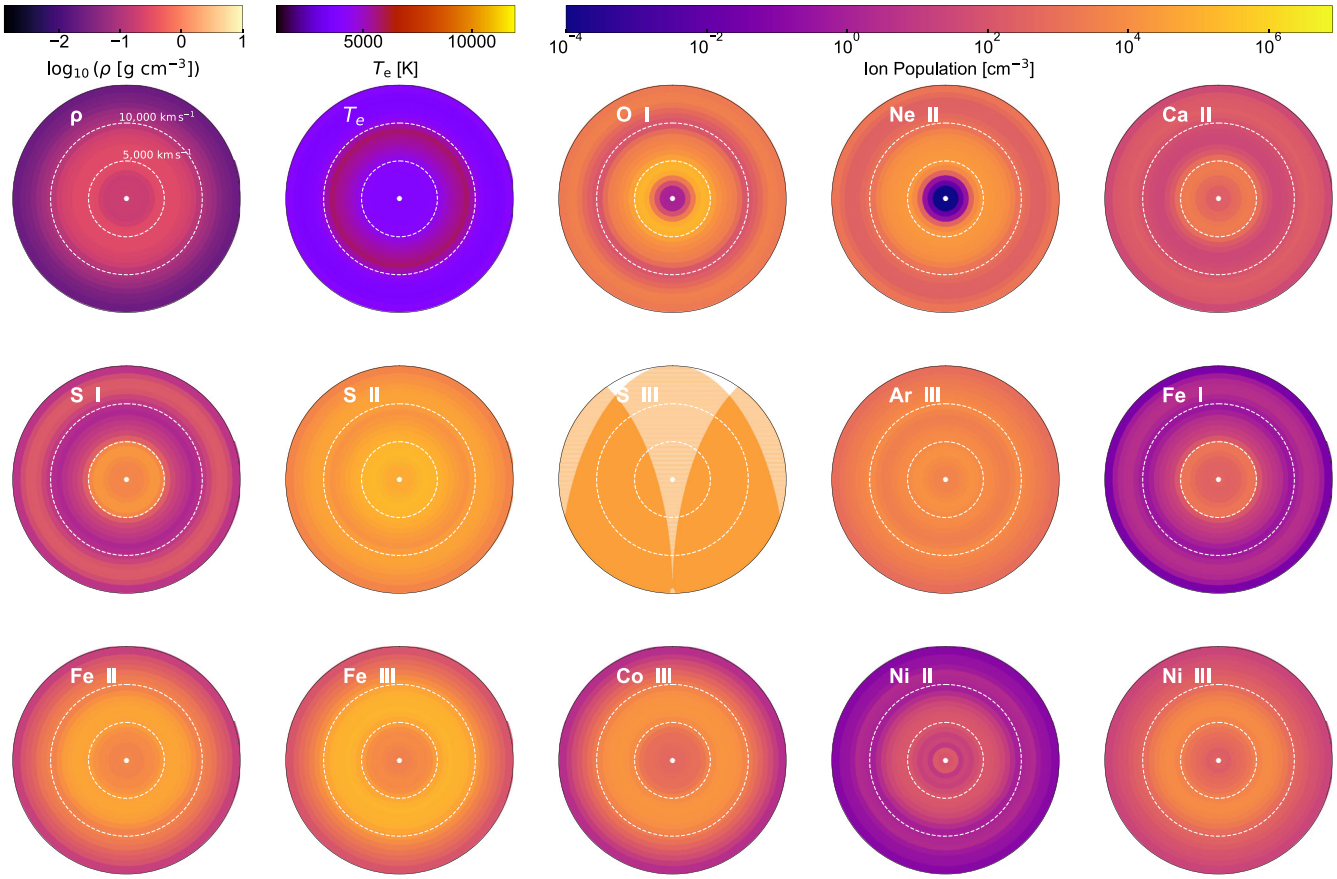

Figure 5. Same as Fig. 3, but for the 1DTwoExpl model.

features also differ between the 1D and 3D treatments; the integrated flux of the S III feature between 0.9–1 μ m is around 21 per cent lower in 3D than in 1D. In contrast, the TwoExpl scenario exhibits a stronger sensitivity to multidimensional effects. In the 1DTwoExpl calculation, the integrated flux of the 0.470 μ m Fe III feature is substantially lower than in the 3DTwoExpl model, with the 3D treatment increasing the integrated line flux by approximately 90 per cent. We do however note that there is still a small amount of opacity in this region in both the 1D and 3D calculation. Other features, such as the Co III emission at 0.589 μ m, remain largely unchanged between 1D and 3D despite Fe and Co being approximately co-spatial. Furthermore, the 3DTwoExpl model shows a reduction of approximately 40 per cent in the integrated flux between 0.69–0.74 μ m when compared to the corresponding 1D calculation, which brings the synthetic spectrum into better agreement with the observations.

While the models predict comparable flux levels across the optical (differing by only ∼10 per cent) and produce broadly similar spectral features, they also exhibit the persistent shortcomings of previous investigations (e.g. L. J. Shingles et al. 2020, 2022; S. Blondin et al. 2023). The most prominent of these is the overionization of Fe, which is most apparent in the region around 0.73 μ m, where both models fail to reproduce the observed blend of Fe II and Ni II at 0.720 and 0.735μ m. Instead, both predict only minor amounts of these singly ionized species (contributing less than 10 per cent to the synthetic spectra in this region; see Table 2), and are instead dominated by a strong Ar III 0.714 μ m feature, consistent with other double-detonation model investigations (e.g. L. J. Shingles et al. 2020; S. Blondin et al. 2023).

Emission features near 0.73 μ m are commonly associated with Ca II in theoretical explosion models (e.g. P. A. Mazzali et al. 2015; S. Blondin, L. Dessart & D. J. Hillier 2018; A. Polin et al. 2021; S. Blondin et al. 2023), and our calculations likewise predict the Ca II lines at 0.729 and 0.732μ m in some of the explosion models. Although Ca II cannot be observationally ruled out for normal SNe Ia in this region (K. Maguire et al. 2018; A. Flörs et al. 2020; L. A. Kwok et al. 2023), its presence has little impact on the inferred Ni/Fe mass ratio (A. Flörs et al. 2020). The 3DTwoExpl model exhibits stronger Ca II emission than the 3DOneExpl model; however, in both cases the emission in this region is dominated by Ar III, rather than the Fe II and Ni II features typically associated with these wavelengths. Prominent Ar III emission is also commonly predicted in nebular-phase explosion models (e.g. L. J. Shingles et al. 2020, 2022; S. Blondin et al. 2023). Although the inclusion of Ca II brings the models into somewhat better agreement with observations, the predicted features are too blue and too narrow to fully explain the discrepancy between observations and simulations on their own. While Ca II emission is generally disfavoured in normal SNe Ia, it may be more consistent with lower mass explosions (e.g. SN 1999by; J. M. Silverman, M. Ganeshalingam & A. V. Filippenko 2013), including sub-$M_{\rm Ch}$ CO WD double-detonation scenarios (see A. Polin et al. 2021, and references therein). However, the 3DOneExpl model, which most closely resembles a standard double-detonation model,

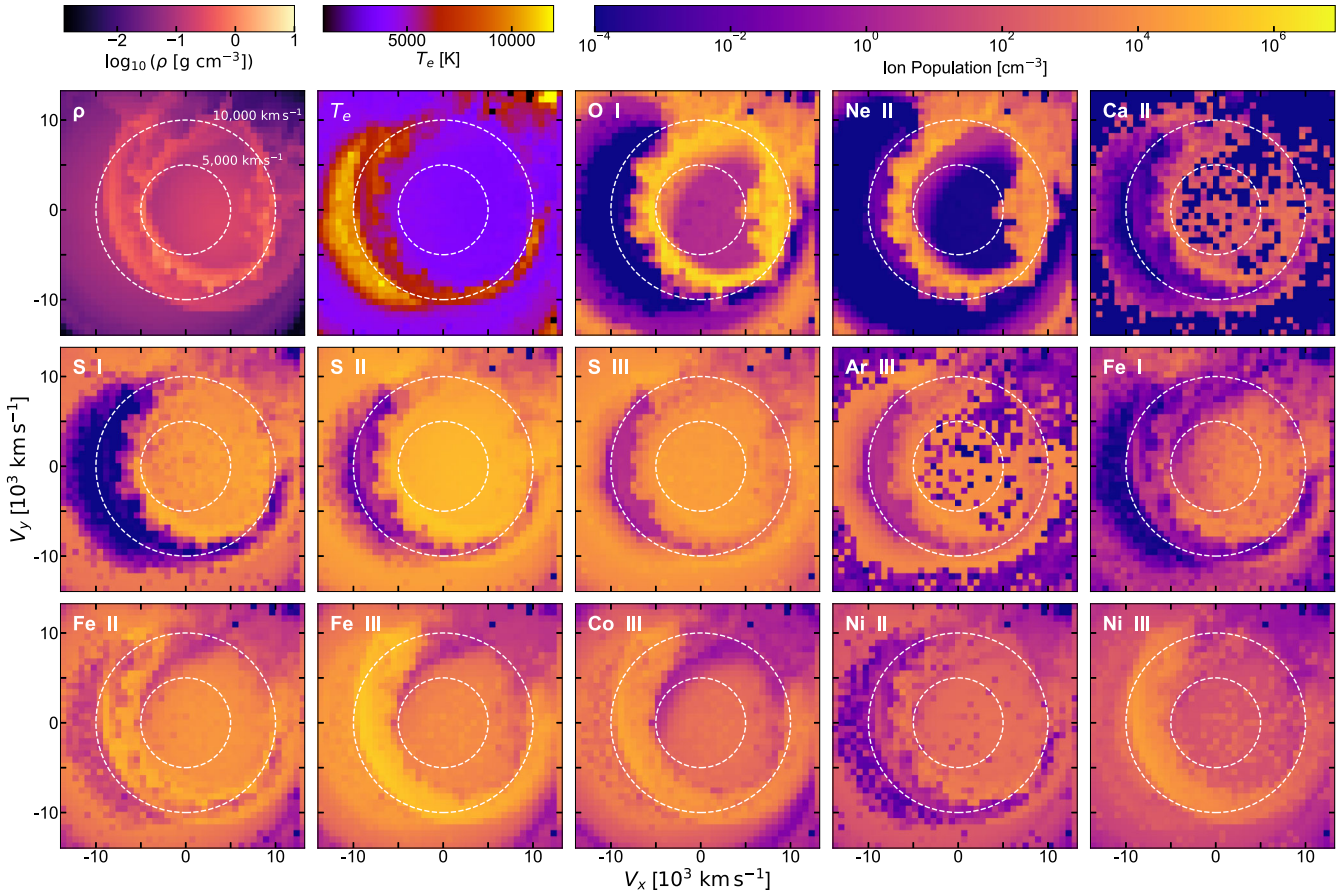

Figure 6. Same as Fig. 4, but for the 3DTwoExpl model.

shows essentially no Ca II contribution in this region. We stress that our models synthesize too much ^{56}Ni to provide a plausible match to subluminous 91bg-like SNe Ia, and that exploring this regime further would require lower mass progenitor systems.

All explosion models except the 1DTwoExpl model, consistently overproduce Fe III relative to Fe II, which is clearly seen in Figs 8–11. We utilize each Monte Carlo packet's last interaction to generate these figures as some packets undergo scattering or fluorescence before escaping which is especially evident in the 3D calculations, where scattering from Fe I is present, and is notably weak in the 1D models. It can be seen that the 3D models generally show more complex line blending in the Fe-dominated features around 0.5 μ m, with increased absorption and a more balanced contribution from Fe I–III. We note that there is a substantial contribution from Fe I in this region and larger Fe I populations in the TwoExpl scenario, when compared to the OneExpl scenario.

3.1.2 NIR comparison

The top panel of Fig. 7 shows the integral of the normalized cumulative flux. In relative terms, significantly more flux emerges in the NIR for the TwoExpl scenario compared to the OneExpl scenario, which exhibits approximately 50 per cent less flux in this region (see Table 1 for a detailed breakdown). This difference in flux can be seen across the NIR spectra in Fig. 2.

The NIR spectra of all models are dominated by IGEs, primarily Fe, with the most substantial contributions arising from Fe III and Fe II. In most models, the dominant IGE feature in terms of peak flux is is the Fe III emission between 2–2.5 μ m. However, the 1DTwoExpl model diverges from this trend, with its strongest feature being Fe II emission at 1.5–1.7 μ m. Ionization effects play a critical role in shaping these differences: the OneExpl scenario is generally more overionized, yielding strong Fe III emission with only minor Fe II contributions (see Figs 8 and 9). In contrast, the 1DTwoExpl model shows improved Fe II and suppressed Fe III emission, producing a weaker 2–2.5 μ m Fe III feature (see Fig. 10). The 3DTwoExpl model possesses a more balanced ionization structure between Fe II and Fe III, though it remains overionized (see Fig. 11). Both scenarios also show distinct Fe I–III distributions: in the 1DOneExpl and 3DOneExpl models, Fe I–III populations are partially cospatial, with Fe I most centrally concentrated, Fe III the most extended, and Fe II being in the intermediate regions (see Figs 3 and 4). While the 1DTwoExpl model (see Fig. 5) mirrors 1DOneExpl model's gradual radial increase in Fe I–III populations, the 3DTwoExpl model (see Fig. 6) contrasts sharply with these distributions: Fe I dominates lower temperature and density regions, while Fe II and Fe III trace higher temperature and density regions, overlapping only marginally with Fe I. Although the exact ion populations do vary from 1D to 3D treatments, we find that the 3DOneExpl model's distributions of Fe I–III are well approximated by spherically averaged ejecta. Critically, however, 3D effects significantly alter the TwoExpl scenarios' distribution of Fe I–III populations throughout the ejecta,

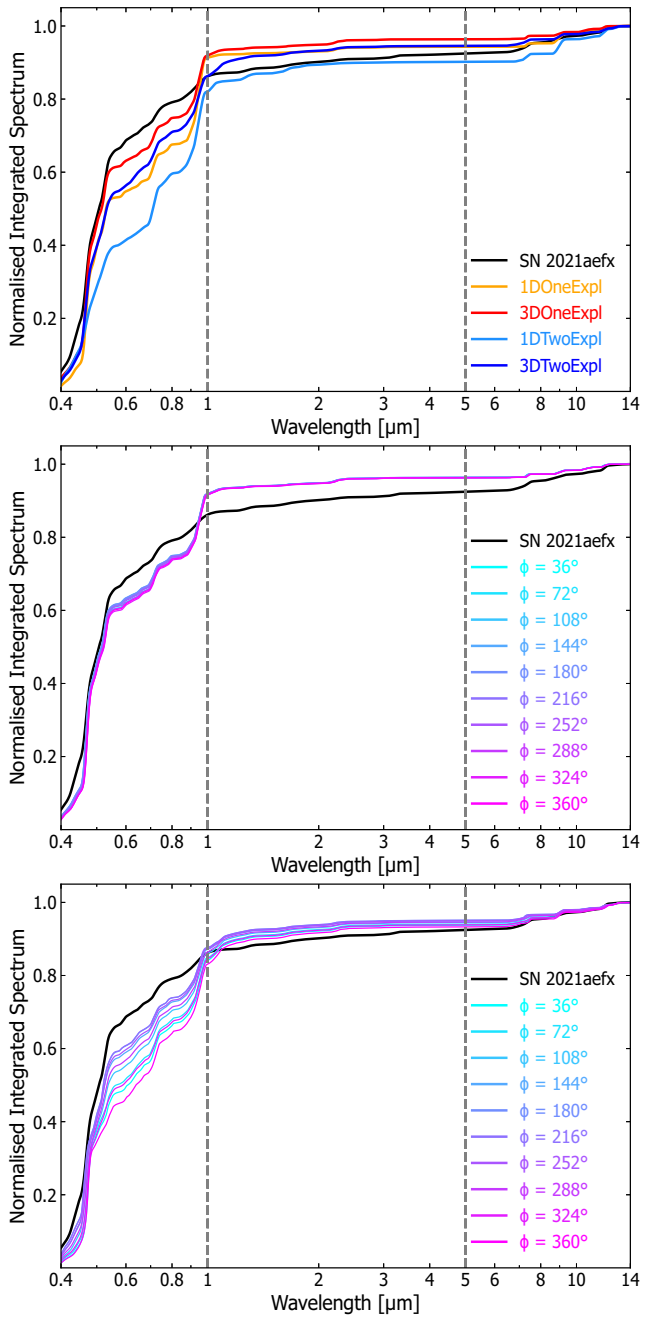

Figure 7. Integral of the normalized cumulative flux per unit wavelength over the range 0.4–14 μm for both explosion scenarios and SN 2021aefx. Dashed vertical lines indicate the boundaries between spectral regions as defined in Section 3. The top panel shows the normalized cumulative flux for the angle-averaged and spherically averaged cases. The middle and bottom panels show the normalized cumulative flux for different observer orientations in the merger plane for the 3DOneExpl and 3DTwoExpl models, respectively.

substantially modifying ionization states and, consequently, the NIR spectra which is most clearly seen by the emergence of an Fe I feature around 1 μm.

It can be seen in Figs 3–6 that the models possess distinctly different Ni II-rich regions within the ejecta: the 1DOneExpl and 3DOneExpl models have centrally concentrated populations, while the 1DTwoExpl and 3DTwoExpl models show more extended distributions at higher velocities. However, none of the models reproduce the strength of the Ni II 1.939 μm feature seen in SN 2021aefx, with the 3DTwoExpl model producing the largest contribution despite the low stable Ni yields in the D[6] scenario (0.016 and 0.018 $M_\odot$ for the OneExpl and TwoExpl scenarios, respectively). As discussed in the context of Fe, the models are overionized, which explains the lack of a 1.939 μm Ni II feature (see Section 3.1.3 for a discussion of an MIR Ni III feature) which is consistent with other double-detention model investigations (S. Blondin et al. 2023).

Another intriguing result in the NIR is the emergence of an S I feature at ∼1 μm in the 3D treatments of the explosion models (Figs 9 and 11). Examination of Fig. 3 shows that for the 1DOneExpl model, S I populations occur predominantly in the least dense outer regions of the ejecta. In the 3DOneExpl model, however, S I populations are approximately two orders of magnitude larger and concentrated in the innermost dense regions (see Fig. 4). This naturally explains the substantially stronger spectral feature in 3D. This inner-velocity component of S I and other IMEs in the 3DOneExpl model originates in the portion of the ejecta where IMEs are swept around the companion. The 1DTwoExpl model possesses only a minor contribution from S I in Fig. 10, which is subdominant to the surrounding IME and IGE features. However, when performing the 3D calculation, the exact stratification and size of the S I populations vary significantly (see Figs 5 and 6). The distribution of S I and other IMEs in the 3DTwoExpl model differs significantly from the 3DOneExpl model. In the 3DTwoExpl model, the detonation of the primary WD produces a shell of IMEs, and the secondary WD's detonation produces a large amount of IMEs in the innermost regions of the ejecta. This stratification of the S I populations in the 3DTwoExpl models is not well approximated by the 1DTwoExpl as it is inherently asymmetric and off-centre; as such, it explains the emergence of the feature in 3D. Although the strength of the feature in the 3DOneExpl model is insufficient to place it in significant tension with observations of SNe Ia, the feature in the 3DTwoExpl model is considerably stronger and inconsistent with SN 2021aefx. However, if the ionization were higher, which may improve other singly ionized features in the NIR, it may produce more S II and bring the model closer to matching the observations.

We note that neither model produces the Ca IV 3.206 μm feature, as this ion is absent from our atomic data set. However, S. Blondin et al. (2023) successfully reproduced this feature using updated atomic data, suggesting both scenarios would likely yield this feature with a similar atomic data set. Beyond the Ca IV feature (omitted from the middle panel of Fig. 2 for clarity but visible in the second panels of Figs 8–11), all models predict negligible flux and fail to match SN 2021aefx's observed low continuum. Instead, they exhibit trace emission from Fe III, Fe II, Ni III, and Si I which aligns with S. Blondin et al. (2023).[8]

3.1.3 Lower MIR comparison (5–14 μm)

We show the 5–30 μm region in the bottom panel of Fig. 2. In this section, we focus on the observed MIR region (5–14 μm), which is dominated by singly ionized Ne and Co, doubly ionized Ar, Ni,

[8]We note S. Blondin et al. (2023) suggest this continuum emission may arise from molecules or dust (see also A. Jerkstrand et al. 2012, for further discussion)

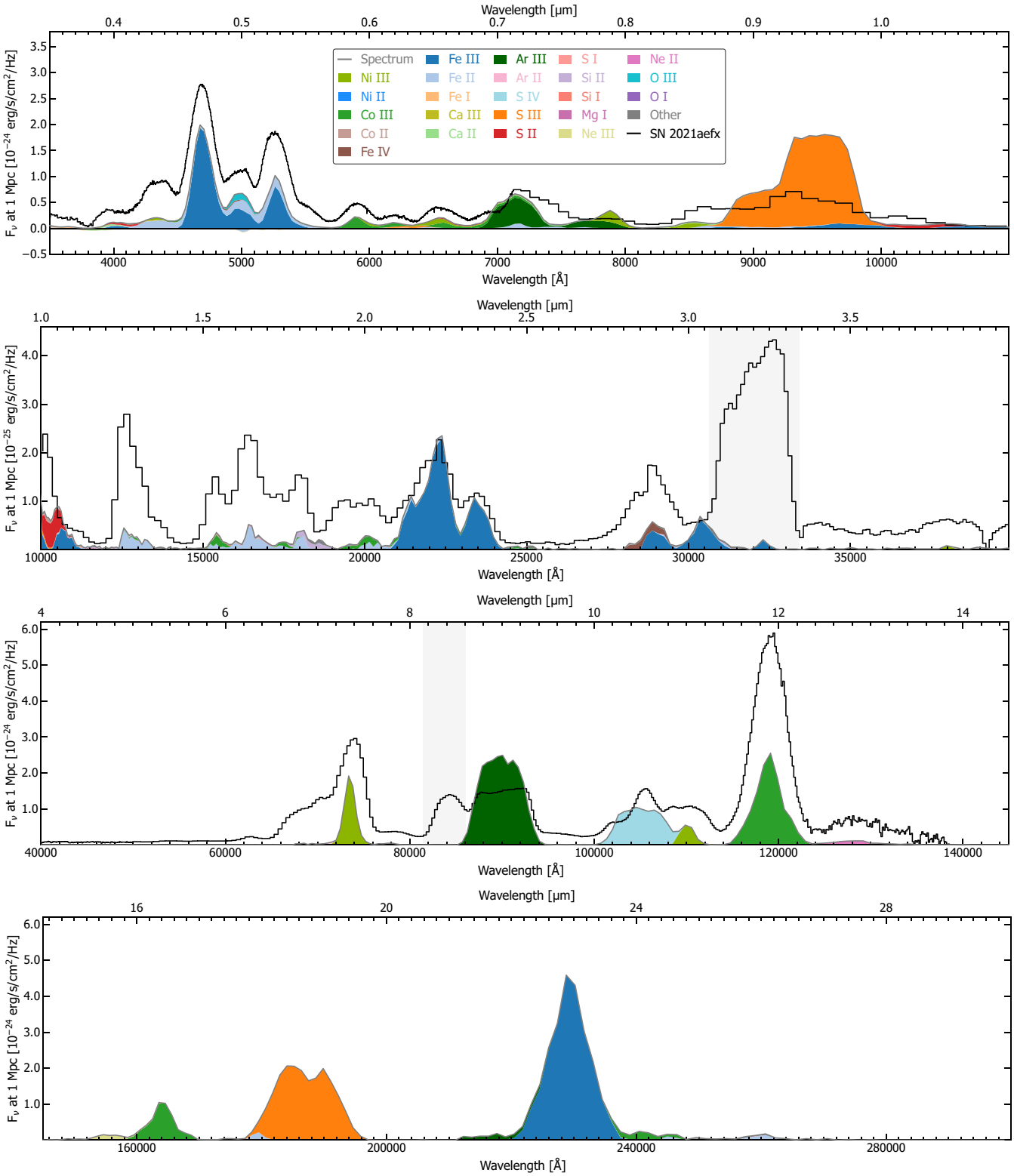

Figure 8. Late-time emission and absorption spectra for the 1DOneExpl model at 270 d across all wavelength ranges, from top to bottom: optical, NIR, lower MIR (∼4–15 μm), and upper MIR (∼15–30 μm). The positive axis indicates the emitting ions, based on each Monte Carlo packet's last interaction. The negative axis shows the corresponding absorption contributions from each ion, which only appear in the optical region. The total spectrum is overlaid as a grey curve, with the shaded regions indicating the contribution of individual ions. Observations of SN 2021aefx (L. A. Kwok et al. 2023) are included for comparison. Note that the shaded regions highlight prominent features that we do not reproduce due to their absence in our atomic data.

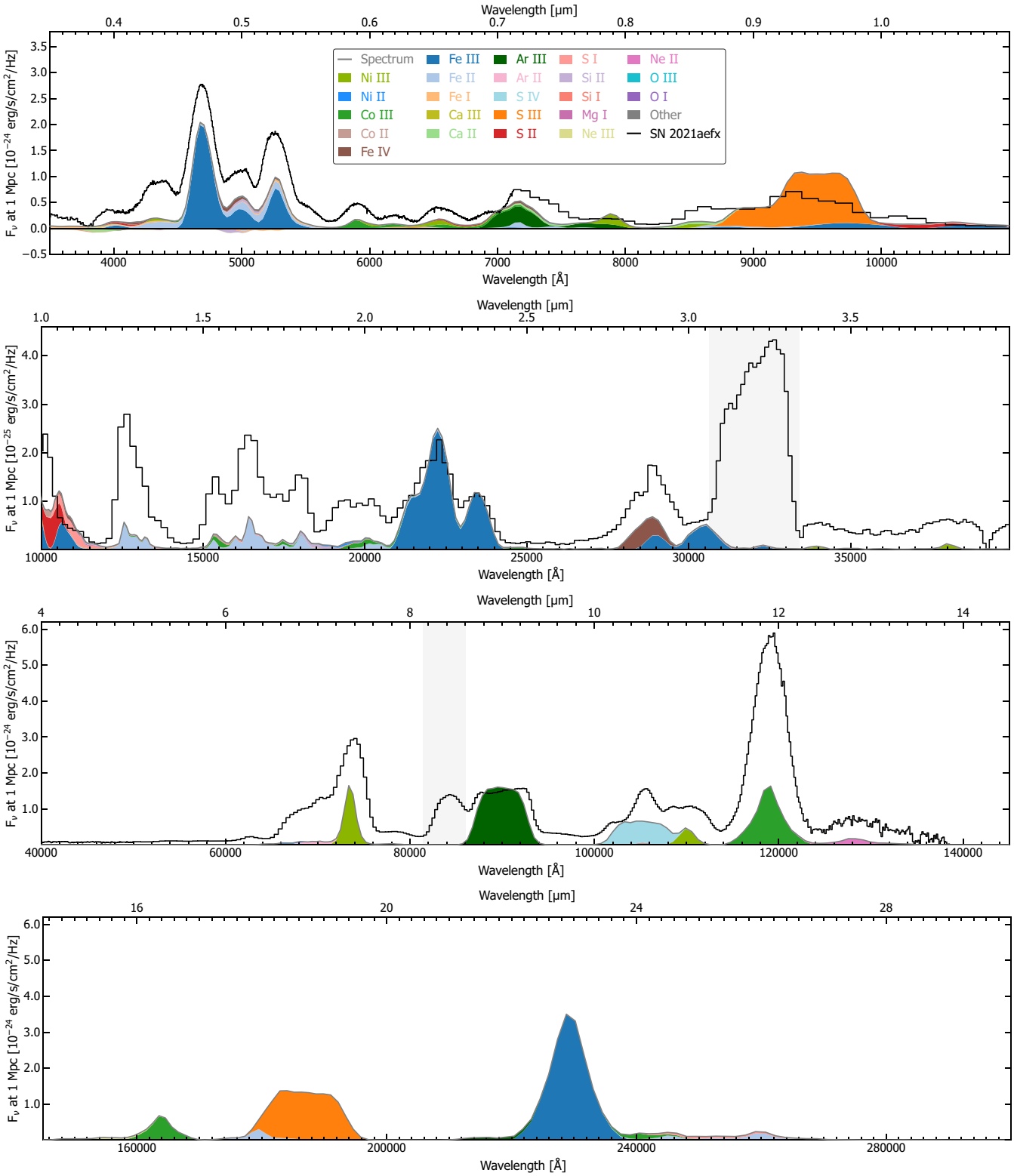

Figure 9. Same as Fig. 8, but for the 3DOneExpl model.

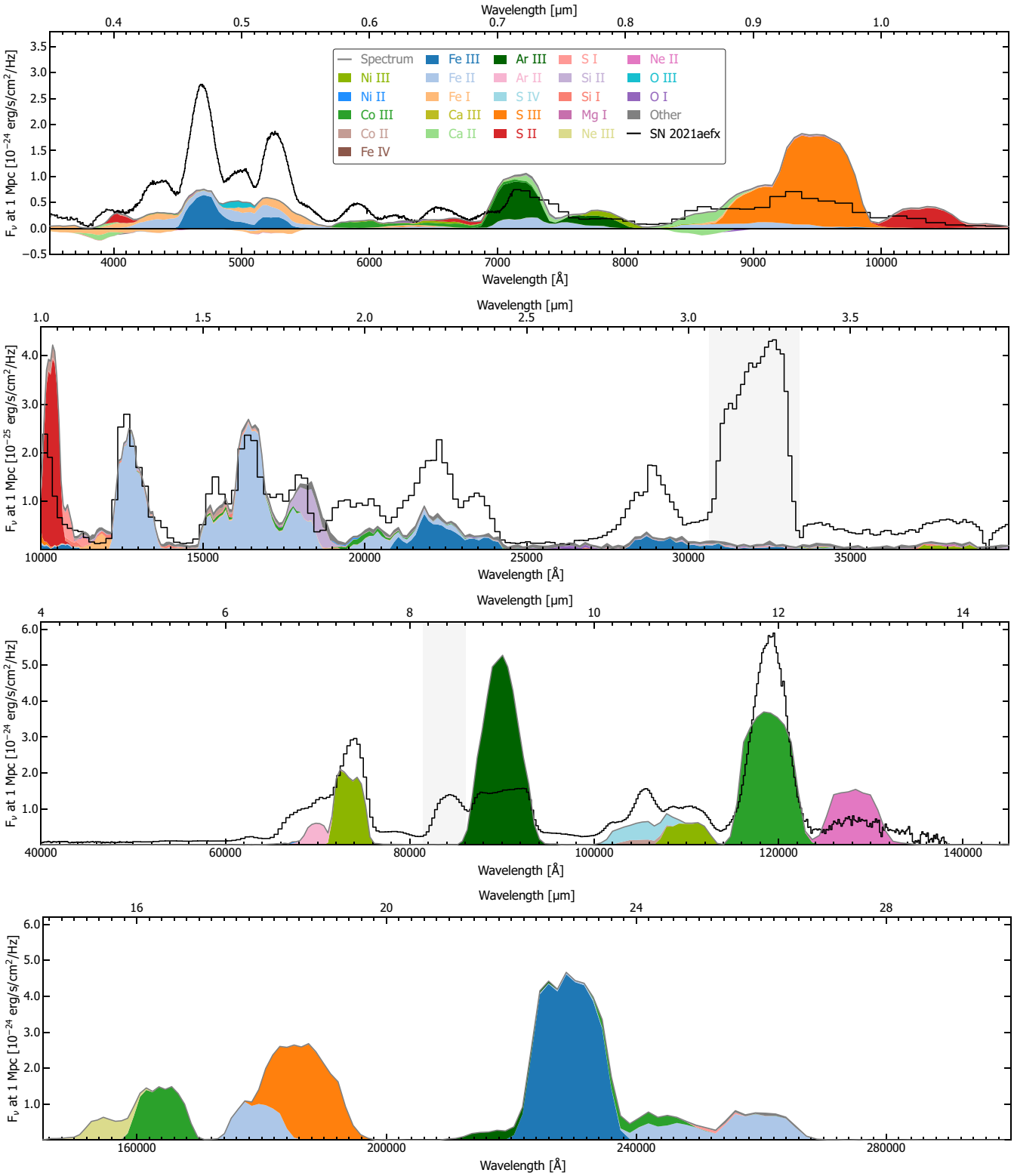

Figure 10. Same as Fig. 8, but for the 1DTwoExpl model.

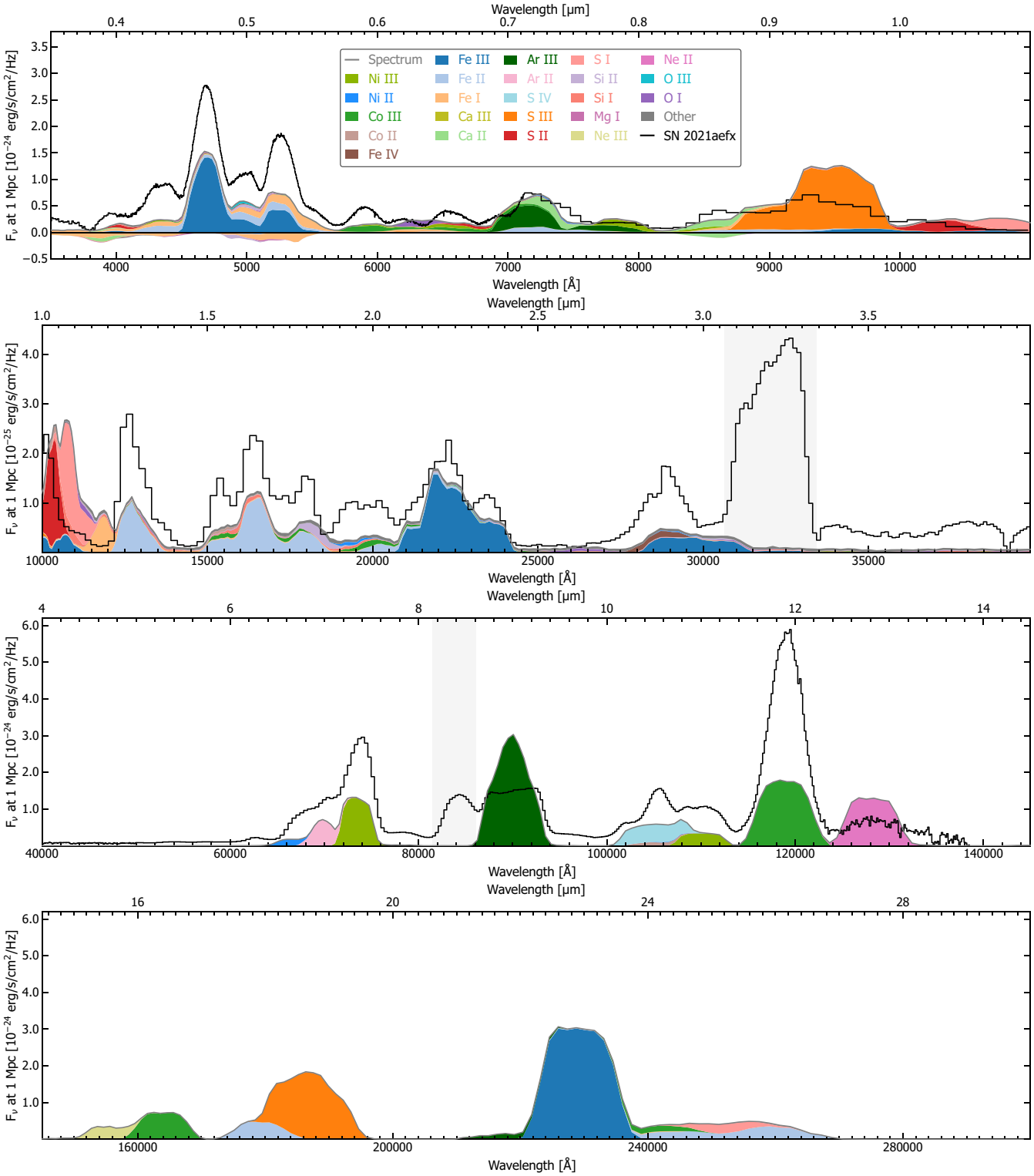

Figure 11. Same as Fig. 8, but for the 3DTwoExpl model.

and Co, and triply ionized S. The models reproduce several MIR features with varied success.[9] Both scenarios exhibit sensitivity to multidimensional effects in the Ni III 7.349 μm, Ar III 8.991 μm, Ni III 11.002 μm, and Co III 11.888 μm features. These effects are strongest in the TwoExpl scenario, where the integrated flux of the Ar III and Co III lines are reduced by ∼38 per cent and ∼54

[9]The Ni IV 8.405 μm transition is absent from our atomic data set (see L. J. Shingles et al. 2020). As such, its absence cannot be used to constrain either scenario. However, it has been produced in nebular calculations (S. Blondin et al. 2023) of double-detonation models (S. Gronow et al. 2021).

per cent, respectively, in the corresponding 3D calculation. In contrast, the OneExpl scenario shows more modest sensitivity to multidimensional effects, with the integrated flux of the Ar III and Co III features decreasing by approximately 6 per cent and 15 per cent, respectively, in the 3D calculation. Similarly to the optical and NIR, singly ionized features such as Ni II 6.636 μm and Ar II 6.985 μm are weak or absent in the OneExpl scenario, while the TwoExpl scenario maintains a more balanced ionization structure.

The 12.8 μm feature of SN 2021aefx was initially attributed to a Ni II 12.73 μm line by L. A. Kwok et al. (2023, see also C. L. Gerardy et al. 2007; C. M. Telesco et al. 2015), but was later identified as Ne II based on radiative transfer calculations of a violent merger (R. Pakmor et al. 2012) and delayed detonation model (I. R. Seitenzahl et al. 2013) by S. Blondin et al. (2023). We note that the violent merger model calculation by S. Blondin et al. (2023) showed a sharply peaked Ne II feature, which was supported by observations of the 03fg-like SN 2022pul (L. A. Kwok et al. 2024). Our calculations show that this feature is composed entirely of Ne II, supporting that identification. The total Ne mass is 0.006 and 0.019 $M_\odot$ in the OneExpl and TwoExpl scenarios, respectively, with Ne II populations approximately four times higher in the latter, explaining its greater strength. We also find that the stratification of Ne differs between the scenarios. In the 3DOneExpl model, Ne II is centrally concentrated and streams outward in one direction, whereas in the 3DTwoExpl model, Ne II is primarily distributed between 5000 and 10 000 km s^{-1}, resulting in a flatter-topped profile.

3.1.4 Upper MIR comparison (14–30 μm)

Across both scenarios the upper MIR region (third panel of Fig. 2; and bottom panels of Figs 8–11) is dominated by several strong emission lines, including Co III 16.391 μm, S III 18.708 μm, and Fe III 22.925 μm, which is consistent with predictions for other model classes (S. Blondin et al. 2023). Our calculations also show contributions from Ne III 15.550 μm, Fe II 17.936 μm, S III 18.713 μm, Ar III 21.832 μm, Co III 24.067 μm, Fe II 24.519 μm, and S I 25.249 μm.

In all models, the Fe III 22.925 μm line is blended on its blue wing with Ar III and on its red wing with Co III. In the TwoExpl scenario, it is further contaminated by Fe II. Nevertheless, even with this blending, the feature remains well-defined relative to others in the upper MIR. All models in this spectral region exhibit an S III 18.713 μm feature, which is blended with an Fe II feature. This is weakest in the 3DOneExpl and 1DOneExpl models and strongest in the 1DTwoExpl and 3DTwoExpl models, reflecting the underlying ionization balance of the different explosion models.

The Co III 16.391 μm feature is the least blended and appears centrally peaked, although its blue wing overlaps an Ne III feature. This Ne III feature primarily emerges in the TwoExpl scenario, similarly to the emergence of the Ne II 12.815μm feature. Moreover, in the 3DTwoExpl model, Ne II and Ne III are mostly co-spatial (i.e. residing in an asymmetric shell), with the geometry not adequately captured in 1D. This results in differences in the line profiles between the 1D and 3D treatments. Intriguingly, the 3D treatment of the explosion models results in an S I 25.249 μm feature redward of the Co III 24.0607 μm feature. This feature is absent in the 1DOneExpl model and negligible in the 3DOneExpl and 1DTwoExpl models. As such, its emergence in the 3DTwoExpl model mirrors that seen in the NIR.

Although no upper MIR observations are available at 270 d post-explosion, additional spectra of SN 2021aefx were obtained at +323 d (J. M. DerKacy et al. 2023) and +415 d (C. Ashall et al. 2024) past rest-frame *B*-band maximum. As our calculations do not extend to such late epochs, we comment only briefly and qualitatively on how this realization of the D^6 scenario performs. Comparing our models to the +415 d spectrum (see fig. 2 of C. Ashall et al. 2024), we find that the Co III 16.391 μm feature in the OneExpl scenario is too sharply peaked relative to the flatter observed profile, whereas the TwoExpl scenario provides a better match in this respect. The neighbouring Fe II 17.936 μm and S III 18.713 μm features are not well reproduced in either scenario, as both models predict flatter, more top-hat-like profiles rather than the sharply peaked structures seen in the observation. Finally, the Fe III 22.925 μm feature in the OneExpl scenario is more sharply peaked and therefore more consistent with the observations than in the TwoExpl scenario. Note that the exact strength of features will evolve over the ∼ 165 d difference between the epochs of our synthetic spectra and those presented by C. Ashall et al. (2024). Therefore, to make more robust statements regarding the exact strength and line shapes of species, further theoretical modelling at these later epochs would be required, which should also include longer-lived decay chains that become significant at late times (see I. R. Seitenzahl, S. Taubenberger & S. A. Sim 2009).

3.2 3DOneExpl model orientation effects

In this section, we present synthetic spectra for the 3DOneExpl model viewed from different observer orientations within the merger plane (i.e. $\cos(\theta) = 0$, $\phi = 0$–360°), as shown in Fig. 12. These spectra allow us to directly assess how the 3D structure influences observable features. We focus on a selection of prominent IGE and IME features across the optical, NIR, and MIR ranges. These features are chosen for their diagnostic potential in probing the stratification of the ejecta, as illustrated in Fig. 13, which shows how their luminosity, Doppler velocity, and morphology vary with orientation. Crucially, we compare the synthetic spectra from the 3D calculation to those from the corresponding 1D model to highlight the impact of the multidimensional approach (a detailed breakdown of the corresponding transitions for each feature is provided in Table 3).

To quantitatively investigate the variations with rotation of the different IGEs shown in Fig. 13, we fit Gaussian(s) to features and extract the velocity and full width at half maximum (FWHM) for each species, as shown in Fig. 14. Although Gaussians are an imperfect approximation for nebular-phase spectral features – since line profiles are shaped by the underlying distribution of the emitting ejecta and often by the blending of multiple transitions from several species – we adopt Gaussian fitting throughout this work as an empirical method to estimate velocities and understand how the geometry influences the spectra. The OneExpl scenario generally yields features reasonably well described as Gaussian-like (i.e. singly peaked with a symmetric profile). This description is commonly adopted for IGE features, as they are typically expected to be centrally located. We follow a method similar to that used in observational studies: we fit a Gaussian to each emission feature by initially selecting continuum points at the edges of the feature interactively. In cases where a feature consists of a multiplet, such as the Fe III 0.470 μm feature, we

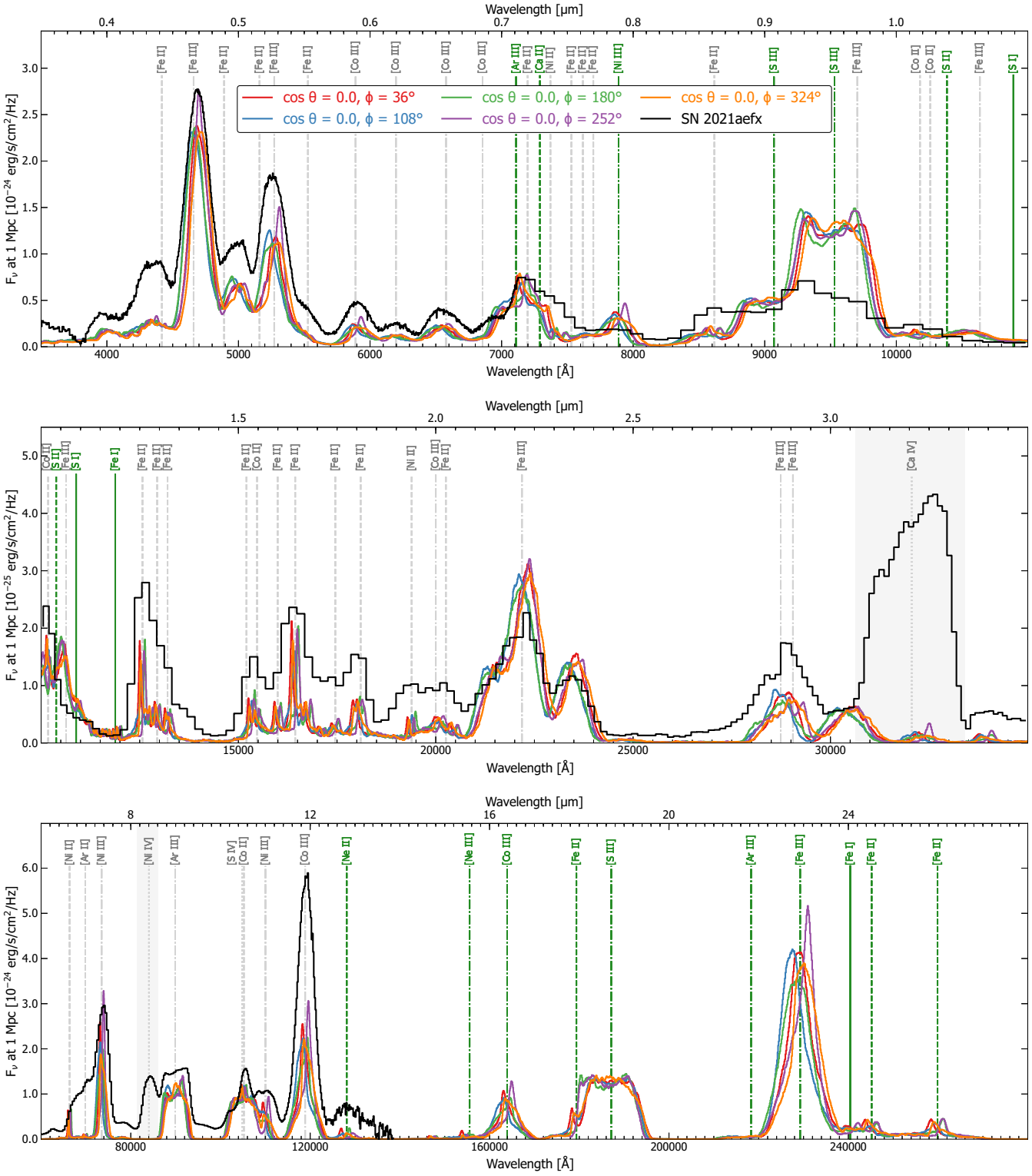

Figure 12. Spectra of the 3DOneExpl model for different viewing angles at 270 d post-explosion for the optical (top), NIR (middle), and MIR (bottom). The lines of sight shown are oriented around the merger plane (i.e. $\cos(\theta) = 0.0$), where the most significant variation in synthetic observables occurs. As in Fig. 2, observed spectra are corrected for redshift and extinction (G. Hosseinzadeh et al. 2022), and all spectra are scaled to a distance of 1 Mpc. Vertical grey lines indicate the rest wavelengths of many prominent features identified by A. Flörs et al. (2020) and L. A. Kwok et al. (2023). In contrast, green lines highlight significant model features that diverge from observations and lie outside the spectral range of SN 2021aefx. The line styles of the vertical lines indicate ionization stages: solid for neutral species, dashed for singly ionized, dash–dotted for doubly ionized, and dotted for triply ionized species. Rest wavelengths identified for SN 2021aefx by L. A. Kwok et al. (2023) are listed in Table 2. Note that a Savitzky–Golay filter has been applied and the shaded grey regions highlight prominent features that we do not reproduce due to their absence in our atomic data.

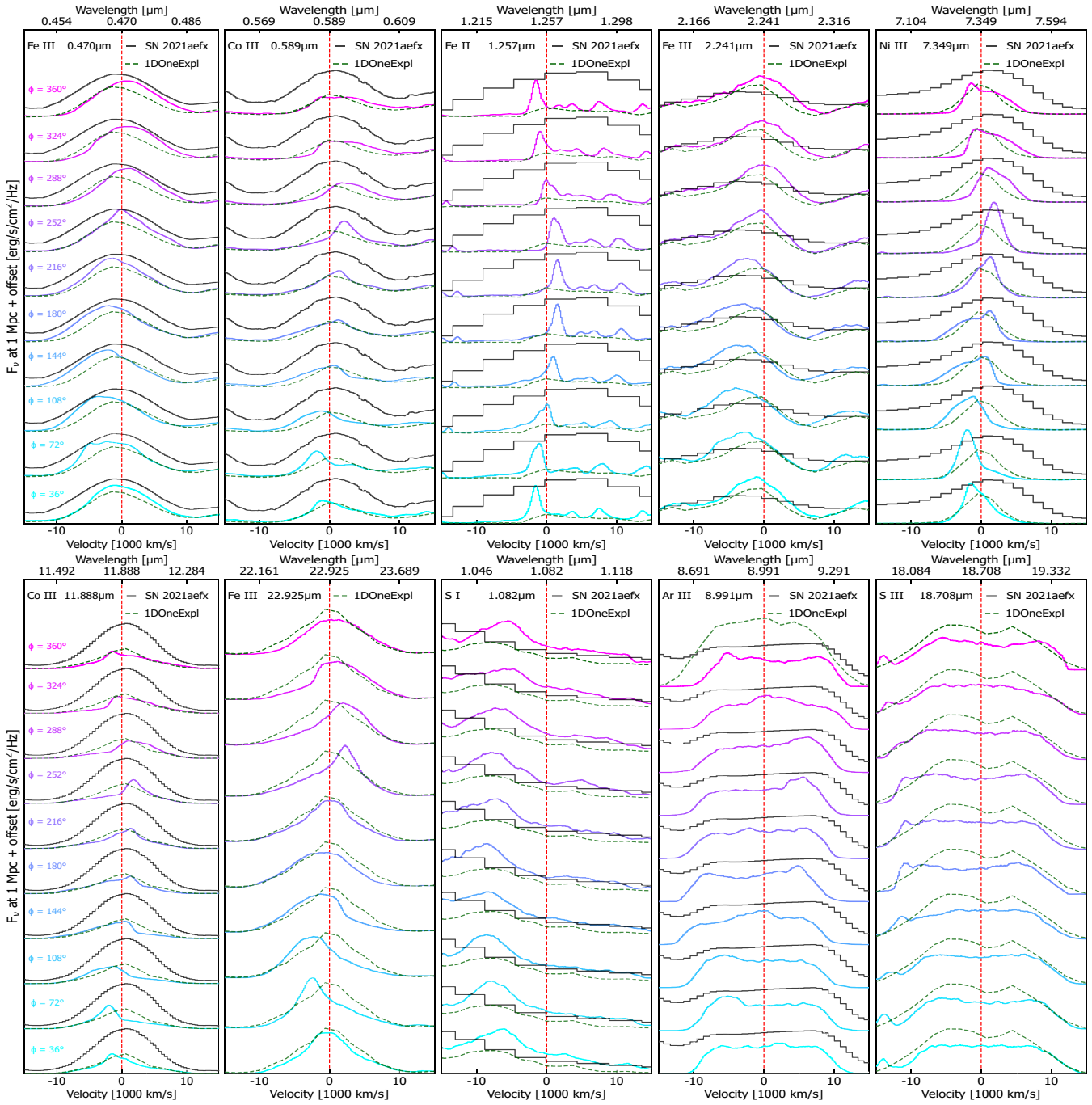

Figure 13. Viewing angle spectra for the 3DOneExpl model at $\cos(\theta) = 0$ (i.e. the merger plane), with the respective orientations (i.e. $\phi = 0$–360°) indicated in the first panel of each row, alongside the corresponding 1D profile from the 1DOneExpl model. Each spectrum is consistently offset, and where possible, compared to the observed spectra of SN 2021aefx (black). We show a set of prominent IGEs and IMEs: Fe III 0.470 μm, Co III 0.589 μm, Fe II 1.257 μm, Fe III 2.241 μm, Ni III 7.349 μm, Co III 11.888 μm, Fe III 22.925 μm, S I 1.082 μm, Ar III 8.991 μm, and S III 18.708 μm, with the dashed verticle line indicating the rest wavelength for reference. See Table 3 for a detailed breakdown of the corresponding transitions.

fit the multiplet with multiple Gaussians. As an alternative, we tested fitting a single Gaussian centred on the gf-weighted mean wavelength of the transitions. This method yielded a comparable velocity trend, although it required a correction to reproduce the expected net blueshift and redshift. To estimate the uncertainties in the velocities and FWHMs, we refit the synthetic spectra three times, varying the initial continuum points, and determined the corresponding standard deviation at each angle. We subsequently adopted the largest standard deviation as the representative error for all points.

3.2.1 Iron group element variations

From Fig. 12, it can be seen that the 3DOneExpl model exhibits distinct variations in line shifts depending on the observer orientation. This behaviour is particularly pronounced in the 0.470 μm

Table 3. Summary of transition(s) and rest wavelengths for emission features displayed in Figs 13 and 16. Where features are due to a multiplet we list the corresponding individual transitions.

Feature	Line(s) (μm)	Rest wavelength (μm)
Fe III	0.461, 0.466, 0.467, 0.470, 0.473, 0.476, 0.477, 0.478	0.470
Co III	0.589	0.589
Fe II	1.257, 1.270, 1.279, 1.294, 1.298, 1.321, 1.328	1.270
Fe III	2.150, 2.218, 2.242, 2.348	2.241
Ni III	7.349	7.349
Co III	11.888	11.888
Fe III	22.925	22.925
S I	1.082	1.082
Ar III	8.991	8.991
S III	18.708	18.708

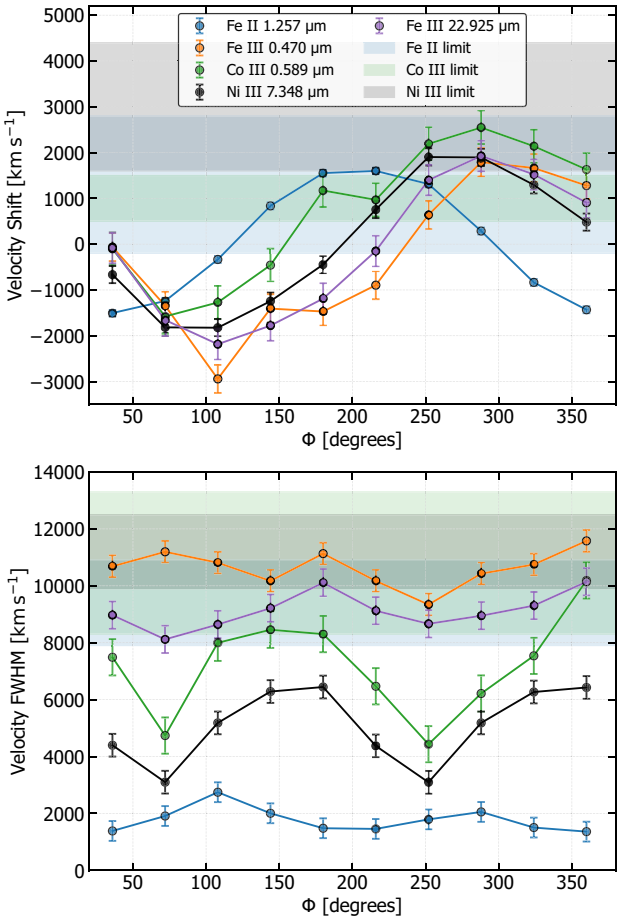

Figure 14. Velocity shifts (top) of the Fe II 1.257 μm, Fe III 0.470 μm, Co III 0.5890 μm, Ni III 7.348 μm and Fe III 22.925 μm features for different observer orientations at $\cos(\theta) = 0$, $\phi = 0$–360° (i.e. the merger plane), and the corresponding FWHM (bottom) for the 3DOneExpl model. The shaded regions indicate the velocity limits determined by L. A. Kwok et al. (2023) for the corresponding features in SN 2021aefx. These velocity limits are shown for the Co III, Ni III, and Fe II features. Note that no limit is shown for Fe III, as no velocity measurement was determined.

Fe III multiplet. Clear Doppler shifts are seen approximately 180° apart (i.e. at $\phi = 108^\circ$ and 252° in Fig. 12), which corresponds to orientations strongly shaped by the secondary WD's survival. This trend becomes even more apparent in Fig. 13, where the feature transitions smoothly from minimal Doppler blueshift at $\phi = 36^\circ$ to a maximum at approximately $\phi = 180^\circ$, and then becomes redshifted with further rotation. A similar trend is observed for the Fe III 2.241 μm multiplet, and it is also evident in the MIR Fe III 22.925 μm feature.

The profiles of features also vary significantly with observer orientation. For example, in Figs 12 and 13, the Fe III 0.470 μm feature at $\phi = 252^\circ$ appears sharply peaked, whereas at $\phi = 360^\circ$ the same feature has a relatively smooth peak. While many orientations produce smoothly varying profiles (i.e. from sharply peaked to more rounded peaks), certain angles reveal more complex structure. For instance, at $\phi = 72^\circ$, the feature appears flatter, with subtle peaks emerging, particularly on the blue wing and near the centre of the profile, which aligns well with specific components of the multiplet. Similar structure can also be observed in the 2.241 μm feature, but it is noticeably absent in the 22.925 μm feature, which corresponds to a single transition and remains sharply peaked at the $\phi = 72^\circ$ viewing angle. These angle-dependent changes in the 0.470 μm Fe III feature differ substantially from the profile predicted by the 1D calculation. As shown in Fig. 13, some orientations (e.g. $\phi = 36^\circ$) closely match the 1D velocity and show a similar corresponding width, other orientations show significant deviations (e.g. $\phi = 252^\circ$).

The spectra exhibit several Co III features across the optical, NIR, and MIR, we focus on the Co III 0.589 μm feature as it is widely observed. We find that the viewing-angle dependence is broadly consistent with that of the Fe III features (see Fig. 13). For example, at $\phi = 36^\circ$, the feature shows negligible Doppler shift, then slowly increasing in its Doppler shift until it reaches a maximum blueshift, then becoming progressively redshifted. However, the viewing angles which correspond to maximum blueshift and redshift differ slightly from those of the 0.470 μm Fe III feature. The 0.589 μm Co III feature exhibits more rapid angular evolution than the Fe III features, reaching a maximum Doppler shift at smaller angles and returning to a near-zero velocity shift by $\phi = 144^\circ$ rather than $\phi = 252^\circ$ which reflects that the stratification of the wake region of the secondary alters the distribution of the ion populations. This behaviour is mirrored in the MIR Co III 11.888 μm and Fe III 22.925μm features, both of which arise from single transitions. We also find that the 0.589 μm Co III feature shows clear orientation-dependent variations in the line wings, central wavelength, and overall profile width that the 1D model does not capture. We stress that these differences between the 3D and 1D profiles exist for all spectral features, as the 3D geometry introduces orientation-dependent variation.

The 3DOneExpl model exhibits a higher ionization than that observed, and thus does not possess a strong Ar II 6.983 μm feature. This leaves the nearby 7.349 μm Ni III feature uncontaminated, enabling a direct probe of the Ni distribution. Across all viewing angles, the 3DOneExpl model predicts a Ni III feature narrower than observed, though its luminosity remains comparable. Notably, the Ni III features are also narrower than the Fe III features in both 1D and 3D calculations, which is consistent with the underlying distribution of populations shown in Figs 3 and 4. We find that the most blueshifted and redshifted profiles occur approximately 180° apart, which is consistent with other IGE features. However, the detailed morphology of the Ni III feature does not always mirror that of the Fe III lines across all viewing angles. For instance, at $\phi = 180°$, the Ni III profile contains distinct velocity components, in contrast to the single blueshifted peak of the Fe III features at 0.470 and 22.925 μm. We attribute this difference in the profiles morphology to the Ni III and Fe III populations not being entirely co-spatial. As shown in Fig. 4, the Ni III distribution is slightly off-centre relative to that of Fe III, with an extended bubble of Ni III (~ 0 to $-10\,000$ km s^{-1}), while the Fe III is more evenly distributed between positive and negative velocities. Finally, we note that the 1D calculation does not accurately reproduce any line-of-sight profile from the 3D model in terms of width, luminosity, or profile morphology.

Both Ni III and Fe III features shown in Fig. 14 follow broadly similar velocity trends, with both showing net maximum blueshifts and redshifts of ~ 2500 km s^{-1}. The Co III feature closely follows the evolution of Ni III, with the most significant deviation occurring at $\phi = 144°$. In contrast to Co III and Ni III, the Fe III 0.470 μm feature does not follow the exact same trend. Instead, the Fe III shows a more gradual evolution. The Fe II 1.257 μm feature also shows a distinctly different velocity evolution, displaying a phase offset of $\sim 90°$ compared to the Fe III feature. Fig. 14 also demonstrates that the FWHMs of Fe II and Fe III differ significantly from one another. These differences in velocities and FWHMs arise from the distributions of their populations within the ejecta not being the same, as shown in Fig. 4. The Fe II populations are primarily concentrated in the innermost ejecta and the region influenced by the wake of the secondary WD, with only minor contributions from the outermost edges, which is significantly different from that of Fe III as those are somewhat more uniform and extended. Fig. 14 also reveals that the FWHMs of the Co III and Ni III clearly show a viewing angle-dependent double-peaked pattern. This arises from an elongated emitting region, which appears broader when aligned with the larger emitting region and narrower when viewed perpendicularly. As a result, two distinct maxima and minima appear. Moreover, the difference between the FWHMs of Co III and Ni III profiles is due to Co III originating from a larger emitting region within the ejecta, reflecting the underlying ion distribution. When comparing the Fe III 0.470 and 22.925 μm features, we find that they exhibit slightly different velocities and FWHMs. Much of these differences are due to the 0.470 μm feature blending with other lines and ionization stages. We note that single transitions are more representative of the models underlying velocity structure, while multiplets involve overlapping profiles.

The velocities and FWHMs of the Fe II, Co III, and Ni III features for SN 2021aefx L. A. Kwok et al. (2023) are plotted as shaded regions in Fig. 14. We find that the predicted velocities for Fe II, Co III, and Ni III from the 3DOneExpl model lie within the observed ranges. However, no single orientation reproduces all observed velocities across all species simultaneously. We note that the $\phi = 216 - 288°$ orientations comes closest, although they yield Ni III or Co III velocities slightly outside those observed. We also find that only the Co III FWHM is consistent with the lower limits reported by L. A. Kwok et al. (2023), and the Ni III and Fe II lines are too narrow to be consistent with observations of SN 2021aefx.

Several large samples of optical and NIR SNe Ia observations already exist (e.g. K. Maeda et al. 2010, 2011; A. Flörs et al. 2018; K. Maguire et al. 2018), but measurements at these wavelengths are affected by line blending, which can introduce substantial uncertainties in inferred velocities and FWHM values. As blending can be severe, any meaningful comparison between explosion models and observations in these regions requires a fully self-consistent fitting procedure applied to both synthetic and observed data. We have not implemented such an approach here, as to fully reconcile the explosion model properties with observed populations, this would require examining significantly more observer orientations and exploring many more explosion models, and as such lies beyond the scope of this work. Furthermore, our current models suffer from overionization of Fe II and Ni II, rendering several key features too weak to provide a satisfactory match to the data; we therefore restrict ourselves to a brief comparison with the overall observational trends seen in SNe Ia populations. Observationally, singly ionized species such as Fe II typically exhibit velocities of $\sim$2000–2500 km s^{-1} and FWHM values of $\sim$6000–9000 km s^{-1} (see fig. 7 of K. Maguire et al. 2018). In the 3DOneExpl model, the velocity spread of singly ionized features is too small, and the predicted FWHM values are lower by roughly a factor of four. For doubly ionized species such as Co III, observed maximum velocity shifts are at most ~ 1000 km s^{-1} with FWHM values of $\sim$8500–11 500 km s^{-1}; in this case, the model Co III maximum velocity shifts are approximately double those observed, while the corresponding FWHM values are, on average, only slightly too small to overlap with the observed sample.

3.2.2 *Intermediate-mass element variation*

In the 3DOneExpl model, IMEs such as S and Ar are predominantly located in the outer layers of the ejecta (see Fig. 1), which is also reflected in the stratification of the ion populations shown in Fig. 4. As IMEs occupy a distinct region of the ejecta compared to IGEs, they exhibit different morphologies and velocity shifts. Examining the optical region in Fig. 12, the S III multiplet feature $\sim$0.93 μm (0.907 and 0.953 μm) shows its strongest blueshift at $\phi = 180°$ and its strongest redshift at $\phi = 36°$. This behaviour differs from the IGEs such as the Fe III 0.470 μm feature, which shows the strongest redshift at $\phi = 252°$. However, the difference in the morphology of the S III feature is more striking than its net redshift or blueshift. Its profile is considerably more flat-topped than the IGE features, as the underlying distribution resembles a hollow shell (see A. Jerkstrand 2017 for a review). As illustrated in Fig. 13, the MIR 18.708 μm S III feature, arising from a single transition with little blending, exhibits this hollow shell distribution more clearly as its profile is distinctly flat-topped across several orientations. Moreover, the 1D profile of this MIR feature is not a good approximation for any 3D observer orientation as no profile exhibits a similar morphology, and all exhibit a lower luminosity than the 1D case

One of the most powerful IME features for diagnostic purposes is the Ar III 8.991 μm line. In our calculation, this feature does not blend with the nearby Ni I line and is well isolated, exhibiting a distinct flat-topped profile that evolves with rotation. As shown in Fig. 13, the feature is nearly entirely flat-topped at $\phi = 36°$, with a small bump emerging on the blue edge at $\phi = 72°$, gradually shifting redward by $\phi = 252°$. As seen in both Figs 1 and 4, most of the Ar III is located in an outer shell; however, some IMEs are distributed from the outer ejecta to the inner ejecta, shaped by the wake of the secondary WD. This wake region produces the bump, which naturally explains the corresponding blueshift if viewed from $\phi = 72°$–$108°$, and a redshift for $\phi = 252°$–$288°$. The 1D model, in comparison to the 3D model, shows a broader profile that does not resemble any of the observer orientations and is notably overluminous. As such, it has been omitted from several line-of-sight comparisons. As noted by L. A. Kwok et al. (2023), the Ar III profile in SN 2021aefx is only marginally sloped. In contrast, our 3DOneExpl model exhibits considerably more structure across many orientations, with $\phi = 36°$ and 216° (separated by 180°) being the most comparable to the morphology of the feature in SN 2021aefx and would not be affected significantly by the wake of the secondary WD. When compared to previously published MIR nebular spectra of the normal SN 2003hv, the peculiar SN 2005df (C. L. Gerardy et al. 2007), and the normal SN 2014J (C. M. Telesco et al. 2015), L. A. Kwok et al. (2023) note that SN 2021aefx exhibits a more symmetric Ar III profile. Therefore, other orientations of the 3DOneExpl model may be more consistent with these MIR spectra.

3.3 3DTwoExpl model orientation effects

In this section, we focus on the viewing-angle variation of the 3DTwoExpl model. Fig. 15 shows the synthetic spectra of the 3DTwoExpl model as viewed from five different orientations within the merger plane (i.e. $\cos(\theta) = 0$, $\phi = 0°$–$360°$). We also investigate a selected set of IGE and IME features across all ten observer orientations in Fig. 16. Finally, we quantitatively compare the velocities and FWHMs of a subset of these IGE features in Fig. 17.

3.3.1 Iron-group element variation

It can be seen in Fig. 15 that the 3DTwoExpl model produces significant variations in both feature velocities and profile morphology depending on the observer's orientation. This variation is considerable across different viewing angles, with velocity shifts approximately double that of the 3DOneExpl model. The optical spectrum displays complex behaviour even among features of the same ionization stage. For example, the central 0.470 μm Fe III feature possesses a narrow peak at its most extreme redshift ($\phi = 36°$), while the Fe III 0.527μ mfeature appears faintest and narrowest at the same orientation. This results from significant absorption and scattering by Fe I (see Section 3.1.1), indicating that the ejecta is not yet fully optically thin and that opacity still influences certain spectral features.

Focusing on the Fe III 0.470 μ m and Co III 0.589 μ m features in Fig. 16, we find that orientations showing a redshift in the Fe III line (e.g. $\phi = 36°$) also exhibit a redshift in the Co III line. Similarly, orientations with a flatter Fe III peak (e.g. $\phi = 144°$) display a comparable profile in the Co III feature. At other angles (e.g. $\phi = 180°$), the 0.470 μ m Fe III multiplet shows a more complex structure which is also seen in the 2.241 μ m Fe III feature. However, in the MIR, the Fe III 22.925 μ m line more closely resembles the Co III 11.888 μ m feature. Additionally, the Fe III 22.925 μ m profile is not centrally peaked at orientations such as $\phi = 252°$. While the 3DOneExpl model showed some differences between MIR and optical Fe III profiles, variations are more pronounced in the 3DTwoExpl model. This change in profile morphology can be attributed to a non-negligible fraction of Fe III residing outside the central ejecta combined with the reduced blending in the MIR.

We find that the more asymmetric 3D structure in the TwoExpl scenario results in more significant variation between lines of sight when compared to those in the OneExpl scenario. A substantial difference between the 1D and 3D treatments appears in the 0.470 μ m feature, which is more luminous and more centrally peaked across 3DTwoExpl model orientations which is also true for the NIR Fe III feature. However, the 1D model can match some features reasonably well, such as the Co III 0.589 μ m feature at flatter-peaked orientations (e.g. $\phi = 288°$). As discussed in Section 3.1, the 3DTwoExpl model reproduces doubly ionized features better than the 1DTwoExpl model but performs worse for singly ionized features. This ionization balance, combined with flatter features and blending with Fe I (see Fig. 11), prevented the extraction of Fe II velocities and FWHMs. Still, the overall larger width features in the 3DTwoExpl model more closely match observations than in the 3DOneExpl scenario.

We also investigate the MIR Ni III 7.349 μ m feature, which in the TwoExpl scenario is slightly contaminated on the blue wing by Ar II. The velocity shifts and morphologies of the Ni III feature closely follow those of the other doubly ionized IGEs (i.e. the Co III and Fe III features), reflecting the similar spatial distributions of their ion populations in the ejecta. We find that the Ni III feature in the 1DTwoExpl model differs significantly from all viewing angles in the 3D calculation, with the 1D model generally producing a broad flatter-topped profile. This behaviour reflects the underlying Ni III distribution in 1DTwoExpl, which is primarily concentrated in a thick outer shell between 5000 and 10 000 km s^{-1} (see Fig. 5). By comparison, the emitting region in the 3DTwoExpl model is not confined to a symmetric outer shell. Consequently, some viewing angles produce more sharply peaked profiles, while others yield broader, relatively flatter-topped features.

It can be seen in Fig. 17 that the Fe III, Co III, and Ni III features show similar maximum blueshifts and redshifts of around 5000 km s^{-1}, approximately double those in the 3DOneExpl model. We also find larger FWHMs in these IGEs compared to the 3DOneExpl model. The Ni III line generally shows the narrowest FWHMs, followed by Co III, while Fe III typically has the broadest FWHMs across most viewing angles, though there are separate angles where Co III overlaps with Ni III and Fe III features. The secondary WD detonation compresses parts of the ejecta on the edge of the bubble into a half-crescent distribution on one side, with the opposite side being dominated by the secondary detonation ash. With this context, the velocity evolution of IGE features can be understood by interpreting Fig. 6. At $\phi = 36°$–$72°$, most of the material is moving away from this observer orientation, which results in a redshift, and the lack of material on this side results in a narrower FWHM. Rotating further results in an orientation where much of the material is still moving away, but the orientation is perpendicular to

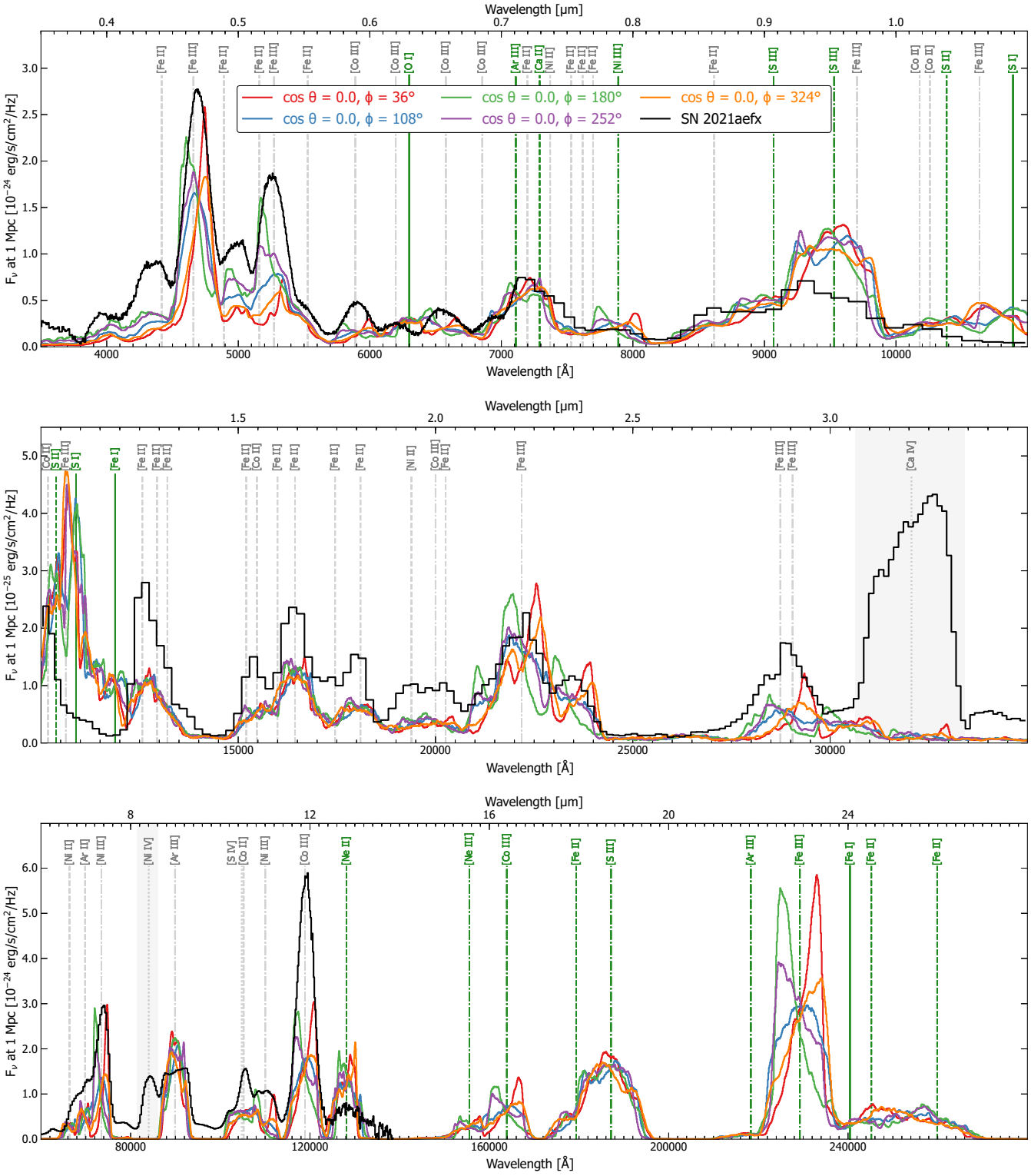

Figure 15. Same as Fig. 12, but for the 3DTwoExpl model.

the elongated compression region, leading to a broader FWHM. Overall, the emitting regions and Doppler velocity shifts in the 3DTwoExpl model are more consistent between species, although their dynamic range is generally larger than in the 3DOneExpl model.

When compared to SN 2021aefx, we find several orientations in which the velocities and emitting regions of Co III and Ni III overlap with those observed. Similar to the 3DOneExpl model, no single viewing angle produces velocity shifts in both Co III and Ni III that align entirely with SN 2021aefx. Moreover, no

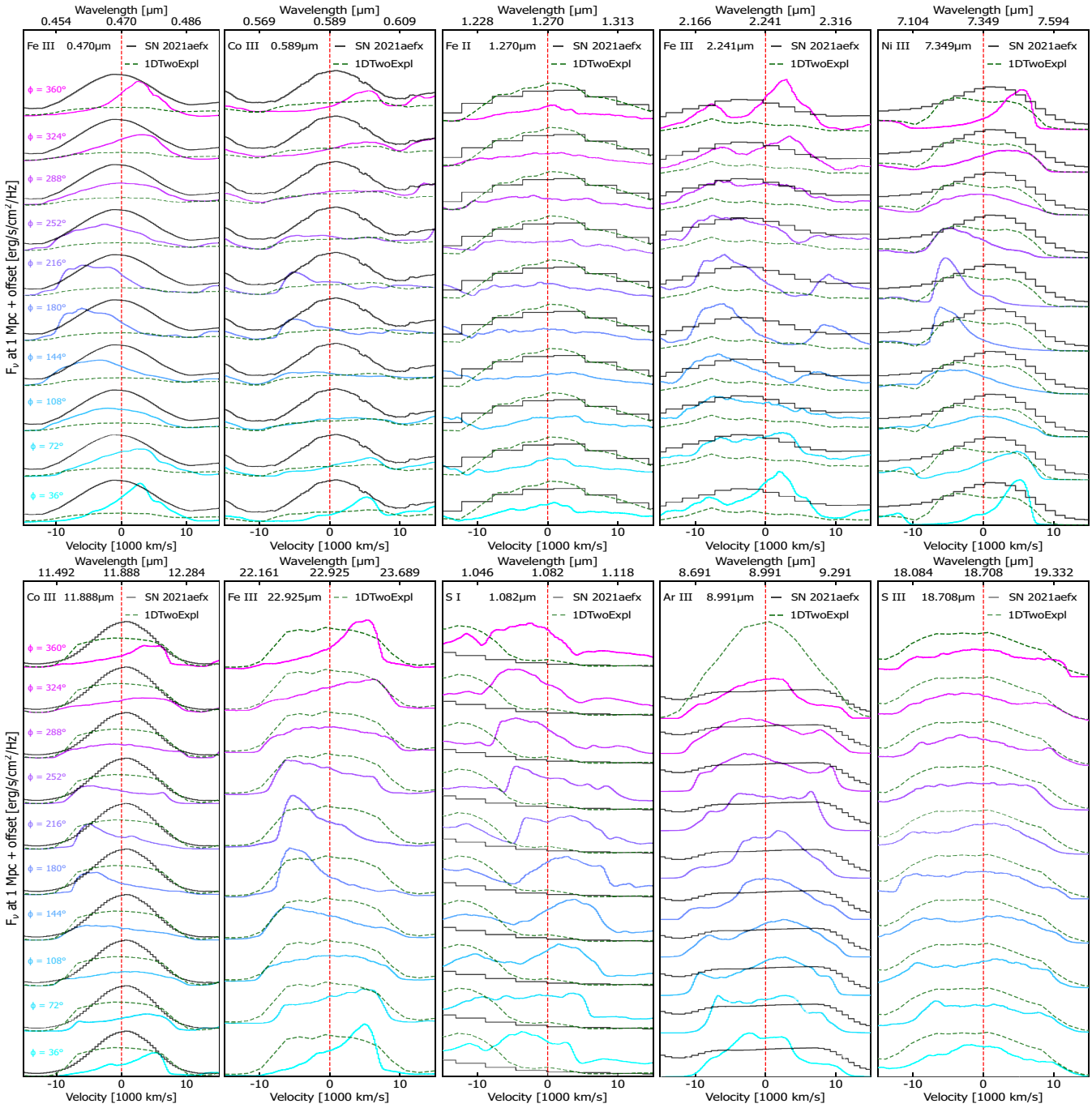

Figure 16. Same as Fig. 13, but for the 3DTwoExpl models viewing angles and 1DTwoExpl model spectra.

individual orientation shows complete agreement in the corresponding FWHMs of the IGEs. These discrepancies arise primarily because the Ni III FWHMs are too narrow. Additionally, on average, there is a smaller net velocity offset between the Co III and Ni III in our calculation than that observed in SN 2021aefx, by approximately 500 km s^{-1}. In general, we find that for several observer orientations, the Ni III emitting region is significantly closer to matching that of SN 2021aefx than in the 3DOneExpl model. However, we stress the need for a broader set of theoretical models and MIR observations.

We now compare to the same observational samples discussed in Section 3.2, in which doubly ionized features such as Co III typically exhibit velocities of $\sim$ 1000 km s^{-1} and FWHM values of $\sim$8500–11 500 km s^{-1}. In the 3DTwoExpl model, the Co III velocities span from $\sim$ 5000 to $\sim-$5000 km s^{-1}, and therefore results in velocity shifts that are approximately five times larger than those observed. However, the average FWHM of the Co III features are $\sim$ 10 000 km s^{-1}, which is broadly consistent with the observed range of $\sim$8500–11 500 km s^{-1}. This suggests that, while the extent of the emitting material is comparable to that inferred from observations, the degree of underlying asymmetry in the model is too pronounced. We also note that for a subset of angles ($\phi = 108^\circ$ and 288°) the FWHM values are much larger than those found in observational samples such as K. Maguire

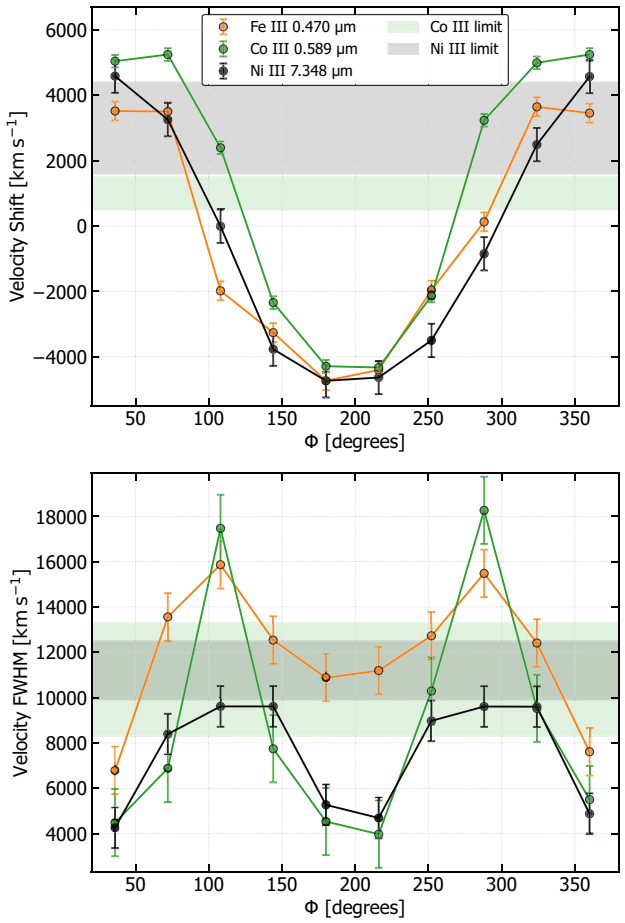

Figure 17. Similar to Fig. 14, but for the Fe III 0.470 μm, Co III 0.5890 μm, and Ni III 7.348 μm features of the 3DTwoExpl model. Note the different velocity scales compared to Fig. 14.

et al. (2018). A more comprehensive examination, incorporating a broader number of explosion models, a wider range of observer orientations, and a self-consistent fitting approach between both synthetic and observed spectra, would be required to robustly assess compatibility of the theoretical models with the observed populations of SNe Ia, and as such lies beyond the scope of the present investigation.

3.3.2 Intermediate-mass element variation

In the 3DTwoExpl model, IMEs are located in the outer and innermost regions of the ejecta (see Figs 1 and 6) with the secondary detonation increasing the abundance of IMEs such as S and Ar by approximately 50 per cent. This distribution arises from the detonation of both the primary and secondary WDs and their detonation timings. During the primary detonation, the secondary remains intact, causing IMEs from the primary to be located in the outer ejecta. Subsequently, the secondary detonation produces a significant amount of IMEs in the innermost regions of the ejecta. As such, the resulting stratification of IMEs is markedly different from the 3DOneExpl model.

The Ar III 8.991 μm feature exhibits substantial variation across different orientations. For instance, at $\phi = 72^\circ$, the model predicts a profile much closer to being entirely flat-topped, while $\phi = 216^\circ$ yields a profile that diverges significantly from being entirely flat-topped. The complexity of the Ar III feature arises from its distribution throughout the ejecta (see Figs 1 and 6), which is neither entirely confined to the outer shell (which would produce a flat-topped profile) nor completely centralized (which would result in a sharply peaked profile). Moreover, compared to other IMEs such as S III, a greater proportion of Ar III is located in the innermost ejecta compared to the outer ejecta, resulting in a profile morphology less well described as a being entirely flat-topped profile. We find that the 1DTwoExpl model produces an Ar III profile more than twice as luminous as the 3D calculation and particularly centrally peaked, exhibiting only a small flat-topped region at its centre. As such, we exclude it from comparison across many orientations in Fig. 16, as it hinders meaningful comparisons between viewing angles and SN 2021aefx. While some orientations in the 3DTwoExpl model yield a somewhat flatter-topped profile, most orientations do not resemble the feature observed in SN 2021aefx. Instead, the Ar III profile more closely resembles those seen in other MIR SNe Ia (e.g. the normal SN 2003hv and peculiar SN 2005df; C. L. Gerardy et al. 2007).

From Fig. 15, it can be seen that the S III multiplet at 0.93 μm deviates from the Doppler velocity shifts seen in the IGEs, exhibiting significantly less variation in the shifts between different observer orientations. More notably, the feature is more flat-topped than the IGE features across all orientations. However, not all orientations are perfectly flat-topped, as some show additional structure in their profile morphology. We also find that the S III 18.708 μm feature follows broadly similar behaviour to the 0.93 μm feature. As illustrated in Fig. 16, we find that the 1D calculation yields a more luminous S III 18.708 μm line, and no 3D observer orientation reproduces the 1D case in both luminosity and width. Despite these differences, the agreement between the 1D and 3D calculations is generally better for S III than for other doubly ionized IMEs such as Ar III. However, the 1D approximation does not always provide a good representation of other ionization stages of S. In particular, the NIR S I feature emerges strongly only in the 3DTwoExpl model (see Figs 13 and 16) and is entirely absent in the 1D calculation. This feature is also highly sensitive to observer orientation, exhibiting a large variation in velocity shift. The feature shows a distinct redshift at $\phi = 180^\circ$, which can be understood by examining the ion distribution (see Fig. 6). This orientation probes a region with low S I populations due to IGEs compressed by the secondary WD detonation filling that region, and some highly ionized S occupying the region surrounding those compressed IGEs. Contrasting this redshift, orientations such as $\phi = 288^\circ$ show a clear blueshift, caused by the compression region of the primary and secondary detonation ash creating a region with a large amount of S I moving toward that direction. Moreover, the feature exhibits a greater width at angles such as $\phi = 252^\circ$, as this orientation views both the outer shell and the innermost S I populations. In the context of the ionization distributions, the evolution of the velocity and widths of the S I feature can be understood, and provides a clear example of how multidimensional calculations enable the investigation of geometry-dependent information for features not present in 1D calculations. Furthermore, as this feature is absent in observations of SN 2021aefx, it serves as a valuable diagnostic to constrain the model.

4 DISCUSSION AND CONCLUSIONS

We performed both 1D and 3D nebular radiative transfer calculations for the D^6 explosion models developed by R. Pakmor et al.

(2022), where the primary difference between scenarios lies in the fate of the secondary WD. We compared the spectra produced by the 1D and 3D models from 0.35–30 μm to assess the impact of multidirectional effects on the synthetic observables. We also analysed line-of-sight spectra for both explosion scenarios, extracting velocities and FWHMs for IGE features. These were also compared to SN 2021aefx (L. A. Kwok et al. 2023), with a particular focus on how different observer orientations in the 3D calculation compare to those observed. There are four key results from our investigation, as follows:

(i) *Multidimensional structure of explosion models.* We find that a multidimensional treatment of explosion models can significantly affect the luminosity and strength of spectral features, such as the 0.470 μm Fe III feature in the 3DTwoExpl model. Comparing 1D and 3D calculations, the extent of change in the synthetic observables closely reflects the ejecta's underlying asphericity level. Both 1D and 3D models also suffer from overionization ; however, the 3DTwoExpl model generally attains a better ionization balance across Fe I–III, which is reflected in the NIR spectral features. Ion populations can also be notably asymmetric and off-centre, especially in the TwoExpl scenario, where the 3D structure alters ionization and leads to the emergence of S I and Fe I features in the NIR, which are suppressed in the 1D calculation. The OneExpl scenario also shows some sensitivity to multidimensional effects, notably altering fluxes of features such as the MIR 8.991 μm Ar III feature. However, it is generally better approximated by spherically averaged ejecta. As emphasized by R. Pakmor et al. (2024), modern explosion models are inherently multidimensional, and our results strengthen the necessity of performing 3D nebular phase calculations to capture the full diversity in synthetic observables.

(ii) *Orientation-dependent observables.* We have demonstrated the ability to extract line-of-sight spectra from 3D calculations, allowing us to investigate velocity shifts, FWHM variations, and diversity in profile morphologies of key nebular-phase features. Across several features, the angle-averaged spectra fail to capture the luminosity, width, velocity, or morphology of any observer orientation. In both explosion scenarios, velocity shifts, FWHMs, and feature profiles exhibit distinctive patterns with rotation that can be understood by analysing the underlying distribution of ion populations. As expected, the TwoExpl scenario shows a heightened sensitivity to orientation effects, with velocity shifts approximately double those of the OneExpl scenario. We also find that the FWHMs of Co III and Ni III features are on average about 2000 $\mathrm{km\,s^{-1}}$ larger in the 3DTwoExpl model. However, the 3DOneExpl model still exhibits substantial and detectable variation in velocity and FWHM across different observer orientations, as is evident by the differing trends of Fe II and Fe III features. Importantly, our results show that the innermost geometry shapes the morphology of IME spectral features like the Ar III 8.991 μm feature, with certain viewing angles in both the 3DOneExpl and 3DTwoExpl models producing synthetic spectra that better match the observations of SN 2021aefx than others.

(iii) *Fate of the secondary WD.* The detonation of the secondary WD impacts nebular-phase synthetic observables more significantly than during the photospheric phase (J. M. Pollin et al. 2024), as the average model spectra differ substantially, evident across the optical, NIR, and MIR regions We find other key differences between the scenarios emerge: the 3DOneExpl model yields overionized and excessively narrow NIR spectra, inconsistent with SN 2021aefx and typical nebular-phase SNe Ia. In contrast, the 3DTwoExpl model more accurately reproduces the observed NIR flux, but introduces discrepancies, including the absence of sharply peaked Co III features, the presence of a strong NIR S I feature, and an MIR Ar III feature that lacks the expected flat-topped profile. While viewing-angle variations in the 3DTwoExpl model can bring the Ar III feature closer to being somewhat flat-topped, we tentatively favour the 3DOneExpl model as a more plausible candidate for normal SNe Ia than this realization of the 3DTwoExpl model. Conversely, the weak optical O I, and strong MIR Ne II feature suggest that the 3DTwoExpl model may be a better match for peculiar 02es-like (e.g. SN 2010lp; S. Taubenberger et al. 2013) or 03fg-like SNe Ia (e.g. SN 2022pul; L. A. Kwok et al. 2024) classes. We, however, note that favouring the OneExpl scenario is in tension with the observed population of hypervelocity WDs, which are expected products of the D^6 scenario when the secondary survives and have been regarded as key evidence for the scenario (K. J. Shen et al. 2018b; K. El-Badry et al. 2023; M. A. Hollands et al. 2025). These hypervelocity runaways can currently only account for 2 per cent of SNe Ia (K. J. Shen 2025), suggesting that while the 3DOneExpl model may be responsible for a small subset, it is unlikely to represent the dominant progenitor channel for SNe Ia.

(iv) *Diagnostic potential of the MIR.* As discussed above, the contrasting spectral signatures of explosion models in the MIR provide a valuable means to distinguish between different explosion pathways. This contrasts with the optical and NIR, where interpreting variations is challenging due to blending, particularly in the main optical Fe complex and the 2.24 μm Fe III feature. Consistent with previous investigations (e.g. C. L. Gerardy et al. 2007; S. Blondin et al. 2023), we confirm that no feature is entirely free from contamination, though the level of blending is significantly reduced in the MIR. Moreover, the MIR offers a valuable opportunity to test predictions of both IGE and IME features, such as the Co III 11.888 μm, Ni III 7.349 μm, Ne II 12.815 μm features and, in particular, the 8.991 μm Ar III feature. We find that the MIR viewing-angle spectra of the 3DOneExpl model produce an Ar III feature more consistent with observations, whereas only specific orientations in the 3DTwoExpl model produce a feature that somewhat resembles SN 2021aefx. This suggests that while centrally located IMEs cannot be entirely ruled out, their presence tends to result in more complex feature morphologies. These conclusions are only possible due to MIR observations, where reduced blending offers strong diagnostic power and allows for a clearer probe of IMEs than optical or NIR wavelengths.

Our multidimensional simulations reveal that a 3D treatment of explosion models can produce spectral features absent in 1D calculations, while also revealing systematic variations in these features depending on the viewing angle, including velocity shifts, FWHMs, and changes in feature morphology. These variations arise from asymmetries in the innermost ejecta and show how different observer orientations can give rise to distinct IGE and IME features. Together, these results show that 3D effects reshape which ions dominate nebular-phase spectra and allow for the determination of model-dependent orientation signatures. Hence, to identify which progenitor channel(s) are most likely to create SNe Ia, it is paramount to investigate a suite of explosion models and compare their spectral variations with samples of observed SNe Ia. We note that ground-based surveys have produced high-quality samples of optical and NIR spectra of SNe Ia (e.g. K. Maeda et al. 2010; J. M. Silverman et al. 2013; M. J. Childress et al.

2015; C. S. Black, R. A. Fesen & J. T. Parrent 2016; K. Maguire et al. 2016, 2018; A. Flörs et al. 2020), which provide opportunities to test 3D explosion models already. Combining these samples with future observations, particularly those from *JWST,* will be critical for thoroughly assessing the optical, NIR and MIR spectra produced by multidimensional models. Our investigation indicates that both D^6 models generated by R. Pakmor et al. (2022) may represent plausible pathways capable of producing normal SNe Ia; however, as discussed, each model faces similar challenges, in particular the underproduction of singly ionized features. Nevertheless, we stress that neither pathway can be definitively ruled out based on a single realization alone, which currently possesses a somewhat artificial initial distribution of helium and in which the detonation of the secondary WD was not entirely self consistent, together with the limited number of *JWST* observations. Of particular interest for furthering our understanding of normal SNe Ia and the D^6 scenario are:

(i) *Parameter space exploration.* A comprehensive suite of nebular-phase calculations for the D^6 scenario are required to assess the role of WD mergers as the progenitors of normal and peculiar SNe Ia. Multidimensional investigations should explore how variations in the following influence explosion geometry and the subsequent impact on nebular spectra (i.e. velocities, FWHMs, and line profiles): different mass pairs, helium shell masses, shell detonation mechanisms (e.g. converging shock, scissors mechanisms, and edge-lit scenarios). Additionally, multidimensional investigation of all classes of explosion models will be essential for determining which nebular features can be reliably reproduced by all progenitor models and which features are truly unique to specific classes of models.

(ii) *Evolution of nebular features.* Future investigations should explore the evolution across multiple epochs in the nebular-phase to determine the impact of additional radioisotopes synthesized in explosion models (I. R. Seitenzahl et al. 2009).

(iii) *Atomic data and ionization challenges.* Updated atomic data sets should be incorporated into future 3D simulations to test model predictions against critical features such as the NIR $\sim$3.5 μm and MIR $\sim$8.5 μm features. Similar to other calculations (see P. Ruiz-Lapuente 1996; P. A. Mazzali et al. 2015; K. D. Wilk, D. J. Hillier & L. Dessart 2018; L. J. Shingles et al. 2020), we also find that the NIR is overionized compared to observations. One possible solution to this discrepancy is clumping (P. A. Mazzali et al. 2020; K. D. Wilk, D. J. Hillier & L. Dessart 2020; S. Blondin et al. 2023) of the ejecta, which results in increased recombination and thus a reduced ionization state bringing synthetic spectra more in line with observations.

ACKNOWLEDGEMENTS

JMP thanks Aysha Aamer for discussions related to the observational spectra and flux conversions. JMP also thanks Kate Maguire for useful discussions during the course of this work. SAS and FPC, acknowledge funding from STFC grant ST/X00094X/1. This work used the DiRAC Memory Intensive service Cosma8 at Durham University, managed by the Institute for Computational Cosmology on behalf of the STFC DiRAC HPC Facility (www.dirac.ac.uk). The DiRAC service at Durham was funded by BEIS, UKRI, and STFC capital funding, Durham University and STFC operations grants. DiRAC is part of the UKRI Digital Research Infrastructure. The authors gratefully acknowledge the Gauss Centre for Supercomputing e.V. (www.gauss-centre.eu) for funding this project by providing computing time on the GCS Supercomputer JUWELS (2021) at Jülich Supercomputing Centre (JSC). JMP acknowledges the support of the Department for Economy (DfE) and the use of Grammarly for proofreading and grammar checking. The work of FKR and AH is supported by the Klaus Tschira Foundation and by the Deutsche Forschungsgemeinschaft (DFG, German Research Foundation) – RO 3676/7-1, project no. 537700965. FKR acknowledges support by the European Union (ERC, ExCEED, project no. 101096243). Views and opinions expressed are, however, those of the authors only and do not necessarily reflect those of the European Union or the European Research Council Executive Agency. Neither the European Union nor the granting authority can be held responsible for them. LJS acknowledges support by the European Research Council (ERC) under the European Union's Horizon 2020 research and innovation program (ERC Advanced Grant KILONOVA no. 885281). AH is a fellow of the International Max Planck Research School for Astronomy and Cosmic Physics at the University of Heidelberg (IMPRS-HD) and acknowledges financial support from IMPRS-HD. CEC is funded by the European Union's Horizon Europe research and innovation programme under the Marie Skłodowska-Curie grant agreement no. 101152610. We acknowledge NUMPY (C. R. Harris et al. 2020), SCIPY (P. Virtanen et al. 2020), MATPOLTLIB (C. R. Harris et al. 2020) and ARTISTOOLS [10] (ARTIS Collaboration 2024a) for data processing and plotting. We also wish to thank the anonymous referees for their constructive comments and helpful suggestions.

DATA AVAILABILITY

The spectra presented here will be made publicly available via the Heidelberg Supernova Model Archive (HESMA; M. Kromer, S. Ohlmann & F. K. Röpke 2017; https://hesma.hits.org). They may also be obtained directly from the corresponding author upon request.

REFERENCES

ARTIS Collaboration, 2024a, artistools, Zenodo, https://doi.org/10.5281/zenodo.14337284
ARTIS Collaboration, 2024b, artis, Zenodo, https://doi.org/10.5281/zenodo.11230916
Anderson L. S., 1989, ApJ, 339, 558
Ashall C. et al., 2022, ApJ, 932, L2
Ashall C. et al., 2024, ApJ, 975, 203
Axelrod T. S., 1980, PhD thesis, University of California, Santa Cruz
Bildsten L., Shen K. J., Weinberg N. N., Nelemans G., 2007, ApJ, 662, L95
Black C. S., Fesen R. A., Parrent J. T., 2016, MNRAS, 462, 649
Blondin S., Dessart L., Hillier D. J., Khokhlov A. M., 2017, MNRAS, 470, 157
Blondin S., Dessart L., Hillier D. J., 2018, MNRAS, 474, 3931
Blondin S., Dessart L., Hillier D. J., Ramsbottom C. A., Storey P. J., 2023, A&A, 678, A170
Boos S. J., Townsley D. M., Shen K. J., Caldwell S., Miles B. J., 2021, ApJ, 919, 126
Boos S. J., Townsley D. M., Shen K. J., 2024, ApJ, 972, 200
Botyánszki J., Kasen D., 2017, ApJ, 845, 176
Bulla M., Sim S. A., Kromer M., 2015, MNRAS, 450, 967
Childress M. J. et al., 2015, MNRAS, 454, 3816
Collins C. E., Gronow S., Sim S. A., Röpke F. K., 2022, MNRAS, 517, 5289

[10] https://github.com/artis-mcrt/artistools/

Collins C. E. et al., 2025, MNRAS, 538, 1289
Das P. et al., 2025, Nat. Astron., 9, 1356
De K. et al., 2019, ApJ, 873, L18
DerKacy J. M. et al., 2023, ApJ, 945, L2
Diamond T. R., Hoeflich P., Gerardy C. L., 2015, ApJ, 806, 107
El-Badry K. et al., 2023, Open J. Astrophys., 6, 28
Fink M., Röpke F. K., Hillebrandt W., Seitenzahl I. R., Sim S. A., Kromer M., 2010, A&A, 514, A53
Flörs A., Spyromilio J., Maguire K., Taubenberger S., Kerzendorf W. E., Dhawan S., 2018, A&A, 620, A200
Flörs A. et al., 2020, MNRAS, 491, 2902
Fransson C., Jerkstrand A., 2015, ApJ, 814, L2
Gerardy C. L. et al., 2007, ApJ, 661, 995
Gronow S., Collins C., Ohlmann S. T., Pakmor R., Kromer M., Seitenzahl I. R., Sim S. A., Röpke F. K., 2020, A&A, 635, A169
Gronow S., Collins C. E., Sim S. A., Röpke F. K., 2021, A&A, 649, A155
Guillochon J., Dan M., Ramirez-Ruiz E., Rosswog S., 2010, ApJ, 709, L64
Harris C. R. et al., 2020, Nature, 585, 357
Hillier D. J., 1990, A&A, 231, 116
Hillier D. J., Miller D. L., 1998, ApJ, 496, 407
Hoeflich P., Khokhlov A., 1996, ApJ, 457, 500
Höflich P., Gerardy C. L., Nomoto K., Motohara K., Fesen R. A., Maeda K., Ohkubo T., Tominaga N., 2004, ApJ, 617, 1258
Holas A. et al., 2025, A&A, 698, A269
Hollands M. A., Shen K. J., Raddi R., Gaensicke B. T., Bauer E. B., Rebassa-Mansergas A., 2025, MNRAS, 541, 2231
Hosseinzadeh G. et al., 2022, ApJ, 933, L45
Hoyle F., Fowler W. A., 1960, ApJ, 132, 565
Iben I. J., Tutukov A. V., 1984, ApJS, 54, 335
JUWELS, 2021, J. Large-scale Res. Fac., 7, A183
Jerkstrand A., 2017, in Alsabti A., Murdin P., eds, Handbook of Supernovae. Springer, Cham, p. 795
Jerkstrand A., Fransson C., Maguire K., Smartt S., Ergon M., Spyromilio J., 2012, A&A, 546, A28
Jiang J.-A. et al., 2017, Nature, 550, 80
Kashyap R., Fisher R., García-Berro E., Aznar-Siguán G., Ji S., Lorén-Aguilar P., 2015, ApJ, 800, L7
Kozma C., Fransson C., 1992, ApJ, 390, 602
Kozma C., Fransson C., Hillebrandt W., Travaglio C., Sollerman J., Reinecke M., Röpke F. K., Spyromilio J., 2005, A&A, 437, 983
Kromer M., Sim S. A., 2009, MNRAS, 398, 1809
Kromer M., Sim S. A., Fink M., Röpke F. K., Seitenzahl I. R., Hillebrandt W., 2010, ApJ, 719, 1067
Kromer M., Ohlmann S., Röpke F. K., 2017, Mem. Soc. Astron. Ital., 88, 312
Kwok L. A. et al., 2023, ApJ, 944, L3
Kwok L. A. et al., 2024, ApJ, 966, 135
Leonard D. C., 2007, ApJ, 670, 1275
Li C., Hillier D. J., Dessart L., 2012, MNRAS, 426, 1671
Liu W., Jeffery D. J., Schultz D. R., 1997, ApJ, 483, L107
Liu Z.-W., Röpke F. K., Han Z., 2023, Res. Astron. Astrophys., 23, 082001
Livne E., 1990, ApJ, 354, L53
Livne E., Arnett D., 1995, ApJ, 452, 62
Livne E., Glasner A. S., 1990, ApJ, 361, 244
Lucy L. B., 2002, A&A, 384, 725
Lucy L. B., 2003, A&A, 403, 261
Lucy L. B., 2005, A&A, 429, 19
Maeda K., Taubenberger S., Sollerman J., Mazzali P. A., Leloudas G., Nomoto K., Motohara K., 2010, ApJ, 708, 1703
Maeda K. et al., 2011, MNRAS, 413, 3075
Maguire K., Taubenberger S., Sullivan M., Mazzali P. A., 2016, MNRAS, 457, 3254
Maguire K. et al., 2018, MNRAS, 477, 3567
Maoz D., Mannucci F., Brandt T. D., 2012, MNRAS, 426, 3282
Maurer I., Jerkstrand A., Mazzali P. A., Taubenberger S., Hachinger S., Kromer M., Sim S., Hillebrandt W., 2011, MNRAS, 418, 1517
Mazzali P. A., Nomoto K., Patat F., Maeda K., 2001, ApJ, 559, 1047
Mazzali P. A. et al., 2015, MNRAS, 450, 2631
Mazzali P. A., Ashall C., Pian E., Stritzinger M. D., Gall C., Phillips M. M., Höflich P., Hsiao E., 2018, MNRAS, 476, 2905
Mazzali P. A. et al., 2020, MNRAS, 494, 2809
Morán-Fraile J., Holas A., Röpke F. K., Pakmor R., Schneider F. R. N., 2024, A&A, 683, A44
Motohara K. et al., 2006, ApJ, 652, L101
Noebauer U. M., Kromer M., Taubenberger S., Baklanov P., Blinnikov S., Sorokina E., Hillebrandt W., 2017, MNRAS, 472, 2787
Nomoto K., 1980, Space Sci. Rev., 27, 563
Nugent P., Baron E., Branch D., Fisher A., Hauschildt P. H., 1997, ApJ, 485, 812
Pakmor R., Kromer M., Taubenberger S., Sim S. A., Röpke F. K., Hillebrandt W., 2012, ApJ, 747, L10
Pakmor R., Kromer M., Taubenberger S., Springel V., 2013, ApJ, 770, L8
Pakmor R. et al., 2022, MNRAS, 517, 5260
Pakmor R., Seitenzahl I. R., Ruiter A. J., Sim S. A., Röpke F. K., Taubenberger S., Bieri R., Blondin S., 2024, A&A, 686, A227
Phillips M. M., 1993, ApJ, 413, L105
Polin A., Nugent P., Kasen D., 2019, ApJ, 873, 84
Polin A., Nugent P., Kasen D., 2021, ApJ, 906, 65
Pollin J. M., Sim S. A., Pakmor R., Callan F. P., Collins C. E., Shingles L. J., Röpke F. K., Srivastav S., 2024, MNRAS, 533, 3036
Ruiter A. J., Seitenzahl I. R., 2025, A&AR, 33, 1
Ruiter A. J., Belczynski K., Fryer C., 2009, ApJ, 699, 2026
Ruiz-Lapuente P., 1996, ApJ, 465, L83
Ruiz-Lapuente P., Lucy L. B., 1992, ApJ, 400, 127
Schlafly E. F., Finkbeiner D. P., 2011, ApJ, 737, 103
Seitenzahl I. R., Taubenberger S., Sim S. A., 2009, MNRAS, 400, 531
Seitenzahl I. R. et al., 2013, MNRAS, 429, 1156
Shen K. J., 2025, ApJ, 982, 6
Shen K. J., Bildsten L., 2009, ApJ, 699, 1365
Shen K. J., Kasen D., Weinberg N. N., Bildsten L., Scannapieco E., 2010, ApJ, 715, 767
Shen K. J., Kasen D., Miles B. J., Townsley D. M., 2018a, ApJ, 854, 52
Shen K. J. et al., 2018b, ApJ, 865, 15
Shen K. J., Blondin S., Kasen D., Dessart L., Townsley D. M., Boos S., Hillier D. J., 2021, ApJ, 909, L18
Shen K. J., Boos S. J., Townsley D. M., 2024, ApJ, 975, 127
Shingles L. J. et al., 2020, MNRAS, 492, 2029
Shingles L. J., Flörs A., Sim S. A., Collins C. E., Röpke F. K., Seitenzahl I. R., Shen K. J., 2022, MNRAS, 512, 6150
Silverman J. M., Ganeshalingam M., Filippenko A. V., 2013, MNRAS, 430, 1030
Sim S. A., 2007, MNRAS, 375, 154
Sim S. A., Röpke F. K., Hillebrandt W., Kromer M., Pakmor R., Fink M., Ruiter A. J., Seitenzahl I. R., 2010, ApJ, 714, L52
Soker N., 2025, Open J. Astrophys., 8, 36
Spyromilio J., Meikle W. P. S., Allen D. A., Graham J. R., 1992, MNRAS, 258, 53P
Taam R. E., 1980, ApJ, 242, 749
Tanikawa A., Nakasato N., Sato Y., Nomoto K., Maeda K., Hachisu I., 2015, ApJ, 807, 40
Tanikawa A., Nomoto K., Nakasato N., 2018, ApJ, 868, 90
Tanikawa A., Nomoto K., Nakasato N., Maeda K., 2019, ApJ, 885, 103
Taubenberger S., Kromer M., Pakmor R., Pignata G., Maeda K., Hachinger S., Leibundgut B., Hillebrandt W., 2013, ApJ, 775, L43
Telesco C. M. et al., 2015, ApJ, 798, 93
Townsley D. M., Miles B. J., Shen K. J., Kasen D., 2019, ApJ, 878, L38
Virtanen P. et al., 2020, Nat. Methods, 17, 261
Whelan J., Iben Icko J., 1973, ApJ, 186, 1007
Wilk K. D., Hillier D. J., Dessart L., 2018, MNRAS, 474, 3187
Wilk K. D., Hillier D. J., Dessart L., 2020, MNRAS, 494, 2221

APPENDIX A: PHOTOIONIZATION TESTING

As noted in Section 2.2, modifications have been made to the treatment of photoionization in ARTIS to facilitate full 3D NLTE

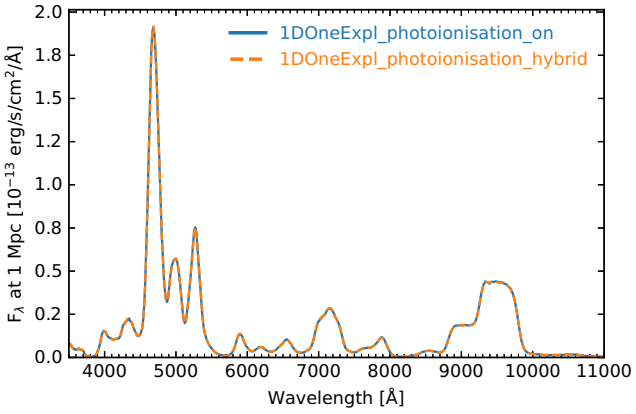

Figure A1. Spectra of the 1DOneExpl model at 270 d post-explosion, shown with full detailed photoionization and in a hybrid mode where detailed photoionization is only applied to levels treated in NLTE.

calculations. ARTIS can employ two distinct methods to determine photoionization coefficients. The first adopts a detailed approach in which specific photoionization Monte Carlo estimators are recorded, following the methodology of L. B. Lucy (2003, eq. 44). The second method uses a radiation field model, which is based on fitting the parameters of dilute *Planck* function models to frequency-binned Monte Carlo estimators and then integrating photoionization cross-sections over this model (see L. J. Shingles et al. 2020). The detailed approach is more accurate since every contribution to the estimator involves the photoionization cross-section at the correct co-moving frequency, but this comes at the expense of involving a distinct estimator for every process considered. In contrast, obtaining values by integrating the radiation field model might sacrifice some accuracy,[11] but can reduce the total number of estimators that need to be recorded.

In our previous 1D nebular studies (L. J. Shingles et al. 2020, 2022), the detailed approach was applied to every photoionization process. However, moving from a 1D model (∼100 grid cells) to a 3D model (∼100 000 grid cells) would result in prohibitively large memory requirements if only this approach is used. We have therefore implemented a hybrid approach. Specifically, the detailed approach is used to obtain photoionization rates for selected photoionization processes (typically those associated with the low-lying states of each ion), while values obtained by integration of the model radiation field are adopted for higher energy levels.

Fig. A1 shows two calculations of the 1DOneExpl model, comparing the following scenario: (1) photoionization rate estimators determined using the detailed approach in all cases and (2) our hybrid scheme in which detailed estimators are only retained for bound–free transitions whose lower levels are included in the NLTE solution (and all other photoionization processes are estimated using the binned radiation-field model). It can be seen that the hybrid scheme effectively reproduces the detailed approach and as such we employ this hybrid scheme throughout our investigation.

[11] Relying on integration of the radiation field model will not resolve any effects of cross-section structure on frequency scales smaller than the frequency bin size of the model

APPENDIX B: COMPUTATIONAL COST AND COMPUTATIONAL DOMAIN

We use ARTIS v2024.5.1 (ARTIS Collaboration 2024b), which has been modified from previous versions to be capable of 3D NLTE nebular calculations for explosion models with up to 50^3 grid cells. As discussed in Section 2.2, our primary 3D nebular simulations employ a 40^3 resolution due to the large computational runtime associated with increasing the number of grid cells. Both 1D and 3D calculations were run on 3072 cores (128 cores per node, 1 TB RAM), with 1D nebular calculations requiring ∼17 000 CPU core hours and the 40^3 simulations averaging ∼473 000 CPU core hours. In total, the combined production cost for two 3D (40^3) and two 1D simulations was ∼980 000 CPU core hours. This cost is primarily dominated by the amount of time needed to update the plasma conditions for each grid cell. Given that we aim to carry out multiple 3D nebular simulations in a future parameter search, any savings in computational costs are extremely valuable. As such, we investigated removing outer grid cells, which are dominated by low-density cells. As such this would make the computational grid 24 000 km s^{-1} instead of 30 000 km s^{-1}.

To assess the impact of this approach, we conducted two lower-resolution simulations. The first is a 3D calculation of the 3DTwoExpl models at a resolution of 25^3 (114 000 CPU core hours). In the second case, we removed the outer grid cells of the 25^3 model to create a 21^3 resolution model (with the outer 2400 km s^{-1} of the ejecta removed; 74 000 CPU core hours). As shown in Fig. B1, we find that removing these outer cells has a negligible effect on the emergent spectra. Based on these results, we performed our main simulations at a resolution of 40^3, which maintains the same inner resolution as our photospheric phase 50^3 calculation (J. M. Pollin et al. 2024), but reduces the total wall-clock time significantly.

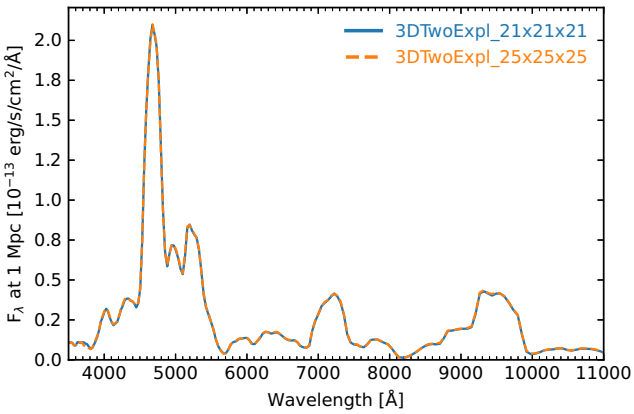

Figure B1. 3D angle-averaged spectra for the 3DTwoExpl model at resolutions of 21^3 and 25^3 at 270 d post-explosion. In the former case, the outer cells were removed from the 25^3 model.

APPENDIX C: ADDITIONAL VIEWING ANGLES

Fig. C1 displays spectra for different viewing angles at constant ϕ with varying azimuthal angles ($\cos(\theta) = 0.0$, 0.4, and 0.8). The 3DOneExpl model shows only minor variations in spectral features. The 3DTwoExpl model, however, displays more pronounced changes, particularly in the luminosity of central optical IGE features, though most features remain relatively similar. While a broader comparison of velocity offsets and profile evolution across viewing angles at these inclinations would be needed

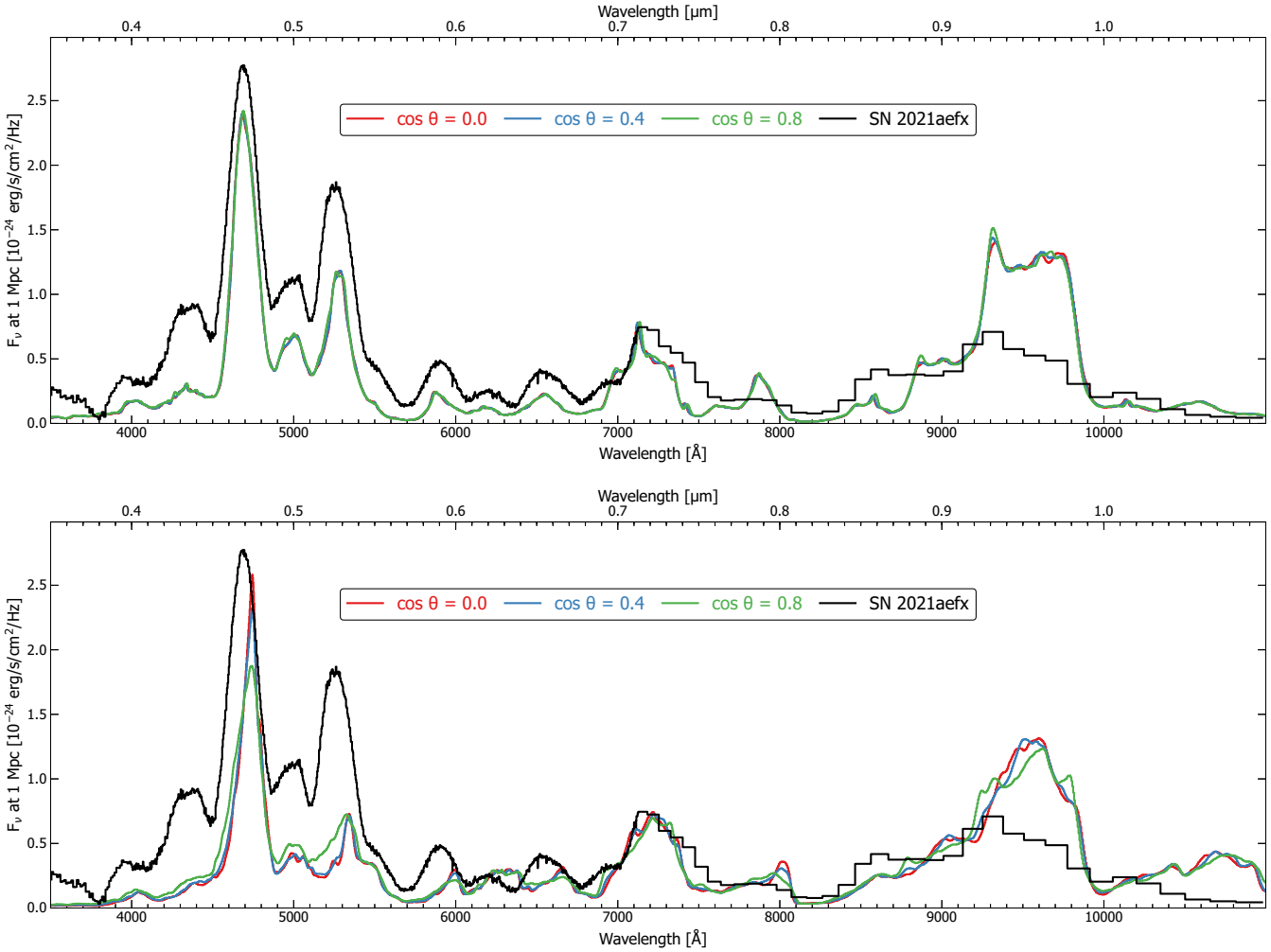

Figure C1. Spectra of the 3DOneExpl (top) and 3DTwoExpl (bottom) models at 270 d post-explosion for different viewing angles. All lines of sight are oriented at $\phi = 36^\circ$ with varying azimuthal angles ($\cos\theta = 0.0$, 0.4, and 0.8). For comparison, we include SN 2021aefx (L. A. Kwok et al. 2023).

for complete observational reconciliation, the overall behaviour of the models can be understood by examining the rotation in ϕ at $\cos(\theta) = 0.0$, as this produces characteristic spectra that capture the key features of the models.

APPENDIX D: ADDITIONAL DENSITY, TEMPERATURE, AND ION DISTRIBUTIONS

As noted in Section 3, we primarily discuss the x–y plane when interpreting spectral features, as the merger plane synthetic observables are the primary focus of our investigation. However, both explosion models are inherently multidimensional and, as such, the 1D temperatures, densities, and ion distributions do not capture the dynamic range of the 3D models. Moreover, the 1D models do not uniquely correspond to the x–y plane of the corresponding 3D calculation. Instead, the 1D radially averaged composition describes the generic properties of the entire ejecta. Therefore, for completeness, we also provide the x–z and y–z slices for the 3DOneExpl model in Figs D1 and D2, and for the 3DTwoExpl models x–z and y–z slices in Figs D3 and D4.

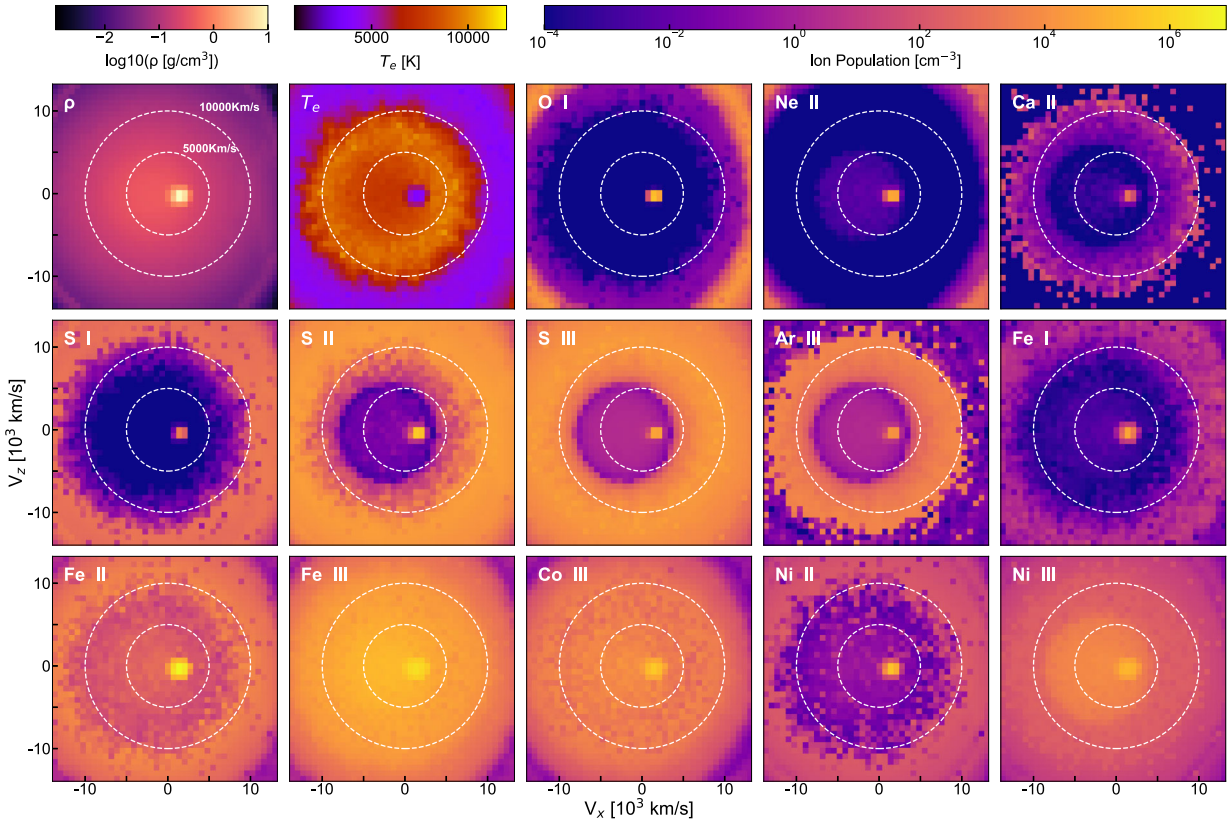

Figure D1. Same as Fig. 4, but for the x–z plane.

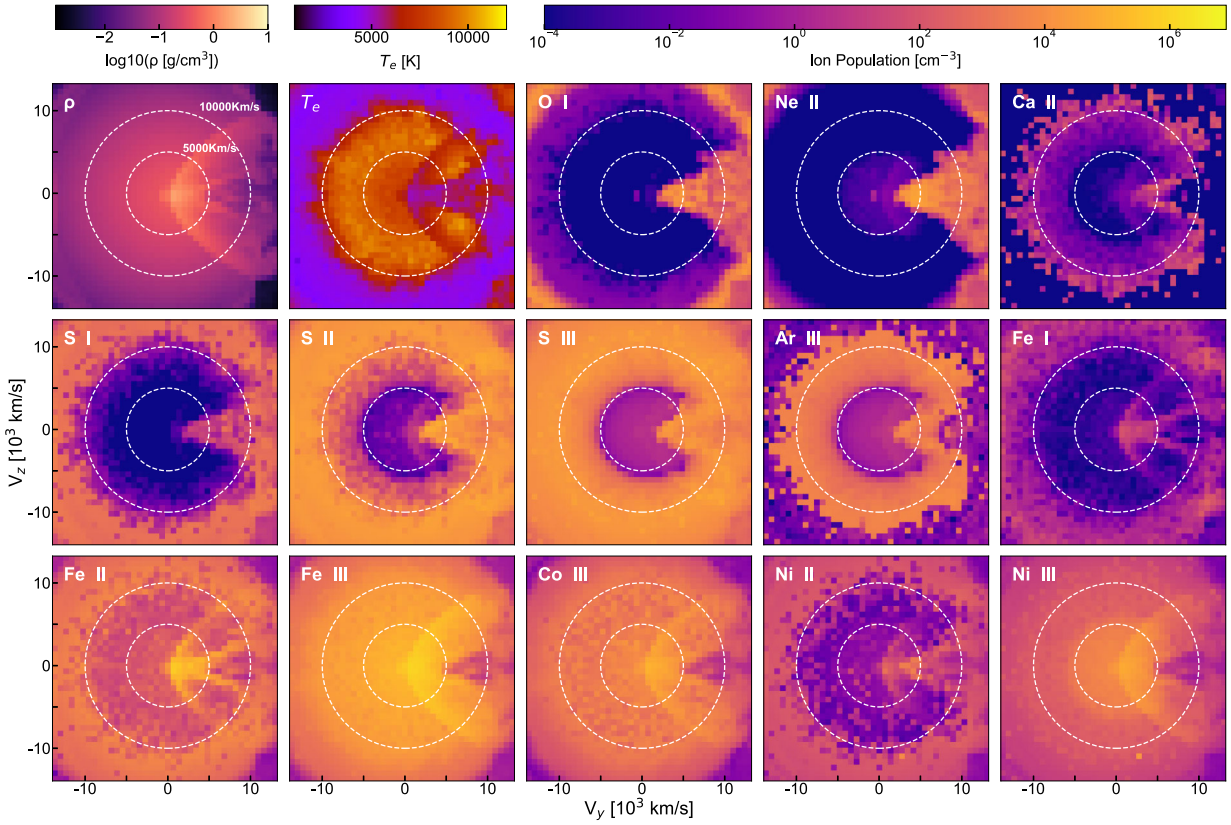

Figure D2. Same as Fig. 4, but for the y–z plane.

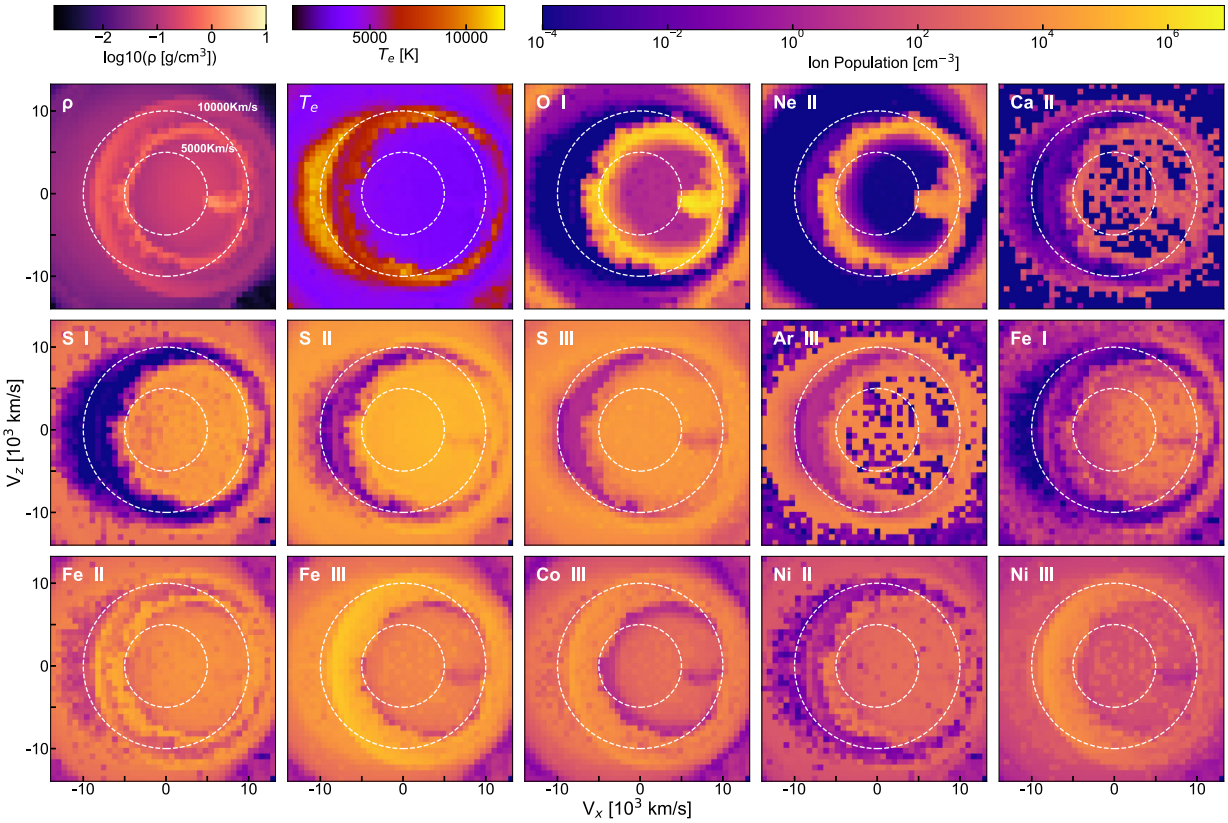

Figure D3. Same as Fig. 6, but for the x–z plane.

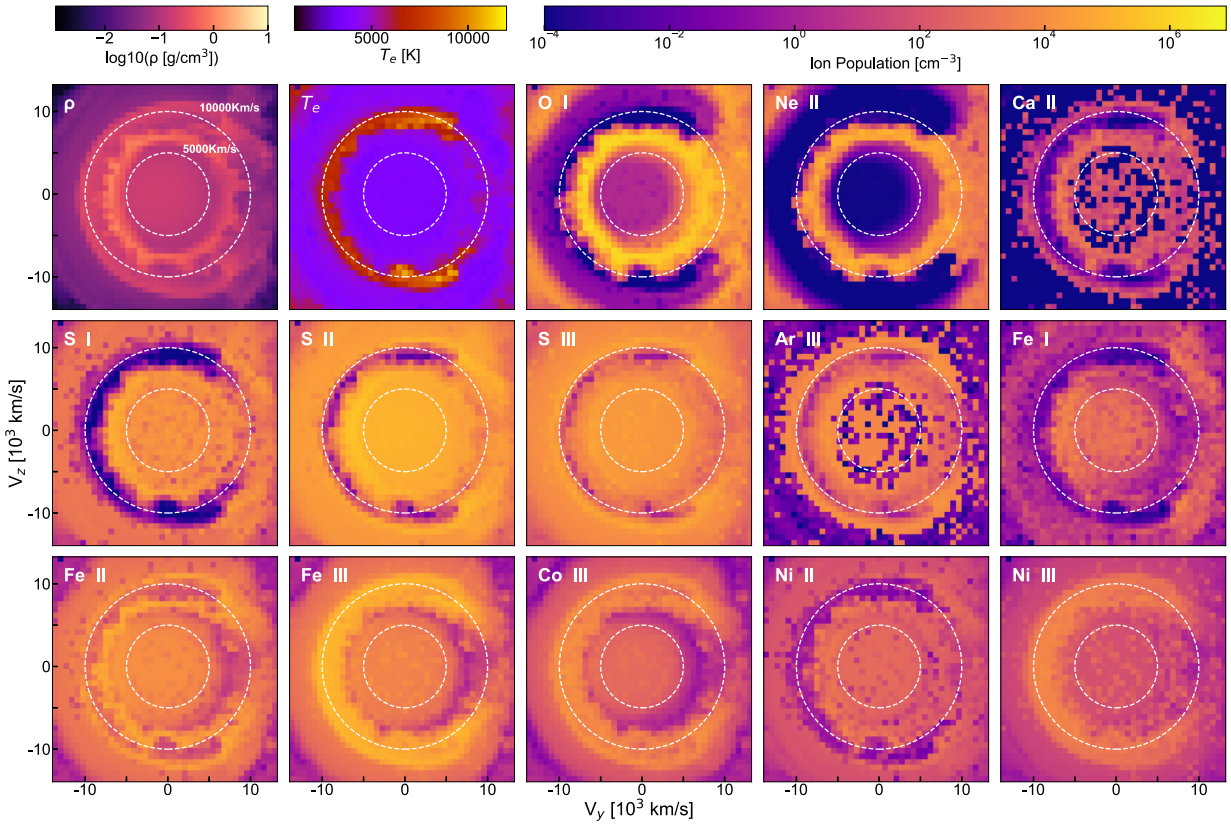

Figure D4. Same as Fig. 6, but for the y–z plane.

This paper has been typeset from a TEX/LATEX file prepared by the author.